

**ESTIMATING OAK TREE BIOMASS USING CANOPY-BASED  
ESTIMATES OF TRUNK DIAMETER DERIVED FROM HIGH  
RESOLUTION SUAS IMAGERY**

A THESIS

Presented to the Department of Geography

California State University, Long Beach

In Partial Fulfillment

of the Requirements for the Degree

Master of Arts in Geography

Committee Members:

Paul Laris, PhD., (Chair)

Scott Winslow, M.A.

Mystyn Mills, PhD.

College Designee:

Sara Schrank, Ph.D.

By Brendan S. Schultheis

B.A., 2022, California State University, Long Beach

August 2024

## ABSTRACT

Methods for quantifying key forest parameters are crucial for numerous applications, but conventional approaches face certain challenges such as costs and accuracy. This thesis aimed to measure aboveground biomass (AGB) using biophysical tree metrics obtained from high-resolution aerial imagery. More specifically, this research explored using canopy-based estimates of trunk diameter to quantify AGB, offering insights into improving forest parameter quantification methods.

Using structure-from-motion (SfM), a 3D model was constructed, and GIS-based techniques were used to extract individual tree data. Remote biometrics were compared to field data, investigating the link between canopy and trunk diameter, a key predictor of AGB. The GIS workflow produced moderately accurate tree polygons, with highly accurate species classification results (84.8%). Canopy metrics from ground and remote data showed a moderate correlation, with canopy area being most consistent. Biomass estimates were reasonably accurate (with the top performing remote estimate being 81.9% accurate) but consistently underestimated AGB.

## ACKNOWLEDGEMENTS

This thesis work was very much a combined effort. I would like to thank all of the students who had a hand collecting the ground data. I have had the pleasure of doing some tough field work, bushwhacking, climbing, and dodging rattlesnakes alongside many peers with the amazing reward of sauntering into the river and sharing laughs and drinks with newfound friends.

This research would not have been possible without Gary Adest, PhD. who not only allowed us to perform research on River Ridge Ranch, but also acted as a wonderful host, friendly tour guide, and sage wisdom giver. Thank you for protecting this wonderful place that has provided so many amazing opportunities and memories, a place I have grown to love.

A special thank you goes out to my Committee Members—Paul Laris, PhD., Scott Winslow, M.A., and Mystyn Mills, PhD.—who supported me through this entire process. I especially want to thank Dr. Laris for all of your guidance and for taking me under your wing. Thank you, Scott, for opening up the world of GIS and remote sensing to me, and as a result putting me on the path I am on today.

Last, but certainly not least, I would like to extend a heartfelt thank you to my people. Mom and dad, thank you so much for everything you've done for me, for all of your support and advice, and for putting me through college. This would not have been possible without you, and I appreciate you more than you'll ever know. Thank you to my brothers for all of your support and for being my biggest fans. Thank you, Talisa, for all the long nights at the café, for providing me with inspiration, and for all of your support. Thanks to mi gatita, Charlotte, for helping me type when I no longer could (because you were obstructing my access to the keyboard).

## TABLE OF CONTENTS

ABSTRACT .....	ii
ACKNOWLEDGEMENTS .....	iii
LIST OF TABLES .....	v
LIST OF FIGURES .....	vi
CHAPTERS .....	
1. INTRODUCTION .....	1
2. REVIEW OF LITERATURE.....	8
3. METHODOLOGY .....	23
4. RESULTS.....	40
5. DISCUSSION AND CONCLUSION.....	50
APPENDICES .....	61
A. IMAGES OF RIVER RIDGE RANCH.....	62
B. PIX4D QUALITY REPORT (RGB).....	65
C. PIX4D QUALITY REPORT (MULTISPECTRAL).....	77
REFERENCES .....	94

## LIST OF TABLES

1. Table 1: Species-specific allometric equations .....	29
2. Table 2: Imagery acquisition parameters .....	31
3. Table 3: Summary statistics of the field data .....	40
4. Table 4: AGB results .....	47
5. Table 5: Accuracy assessment results for ITC workflow .....	49
6. Table 6: Correlation matrix for field-RS canopy .....	49

## LIST OF FIGURES

1. Figure 1: Thesis workflow .....	24
2. Figure 2: Study Site .....	25
3. Figure 3: Sine Method .....	28
4. Figure 4: Overview of River Ridge Ranch .....	28
5. Figure 5: Pix4D processing parameters for RGB imagery .....	32
6. Figure 6: Pix4D processing parameters for MS imagery.....	33
7. Figure 7: Adjusting segmentation results.....	35
8. Figure 8: Regression results for field data .....	42
9. Figure 9: OBIA results .....	43
10. Figure 10: ITC results .....	44
11. Figure 11: Regression results for RS data.....	46
12. Figure 12: Observed tree heights vs RS tree heights .....	48

# CHAPTER 1

## INTRODUCTION

Wooded lands are integral to various aspects of our planet's functioning. Forests and woodlands play a multifaceted role in climate regulation, atmospheric carbon dioxide removal, soil enrichment, erosion mitigation, habitat provision, biodiversity support, and resource supply, including food and wood (Lian et al., 2022; Xu et al., 2020). They are integral to global environmental stability and sustainability. However, forests and woodlands face formidable threats, including anthropogenic deforestation, increasingly frequent and intense wildfires, and prolonged droughts exacerbated by global climate change. These factors contribute to a positive feedback loop that further destabilizes the global climate. The rate at which these changes occur underscores the urgent need to address contributing factors. Not surprisingly, proper management of forest ecosystems has come to play a significant role in numerous initiatives and policies aimed at mitigating climate change.

Programs relating to the reduction of greenhouse gases—particularly carbon offset programs—have become a commonly-applied means of mitigating climate change. Carbon offset programs issue credits to efforts to reduce or eliminate greenhouse gas emissions or sequester carbon dioxide (CO<sub>2</sub>) from the atmosphere and store it elsewhere. Such programs allow polluters to exceed a cap on their greenhouse gas emissions in exchange for climate benefits achieved elsewhere. Polluters effectively offset their CO<sub>2</sub> emissions by purchasing carbon credits, or, in other words, investing money (proportionate to the amount of carbon they emit) into programs that will capture and store atmospheric carbon (Gurgel 2022). For example, a rubber manufacturer that has exceeded its CO<sub>2</sub> emission cap may purchase carbon credits issued to a forest manager who agrees to decrease or suspend timber harvest, thereby allowing the factory to

claim the forest project's generated climate benefits to offset their continued emissions beyond the regulatory limit. Reforestation projects and the reduction or delaying of timber harvests have been at the center of carbon offset programs due to the ability of forest vegetation to sequester carbon from the atmosphere (Lallo et al. 2017). Quantifying forest carbon, however, poses several challenges, including errors in accounting for tree growth timeframes and failure of tree establishment, underestimating emissions during project initiation, and neglecting natural and anthropogenic disturbances (Lefebvre et al., 2021). A recent study examined California's prominent forest carbon offsets program and found that the state's claims regarding climate equivalence are not supported by direct evidence (Badgley et al. 2021). They highlighted a common statistical error known as the ecological fallacy within the structure of California's forest offsets program. The ecological fallacy occurs when group-level characteristics, such as average distribution, are used to draw conclusions about individuals within that group. The ecological fallacy has resulted in systematic overrepresentation of biomass and carbon content in several biomass estimation models that are applied beyond their initial scope, resulting in errors reportedly as high as 240% (Weiskittel et al. 2015). These challenges emphasize the need for continuous monitoring of trees on an individual scale throughout the project duration.

Carbon offset projects represent just one facet of the broader forest management endeavor that relies heavily upon frequent assessments of forest attributes. A host of other initiatives also rely on precise and timely assessments of forest ecosystems, including the Forest Inventory and Analysis (FIA) program, Reducing Emissions from Deforestation and Forest Degradation (REDD) efforts, carbon reduction plans that harness forests as carbon sinks, and the development of accurate climate models that incorporate terrestrial biogeochemical feedback (Iizuka et al. 2017). While forest ecosystems serve as the foundational support for numerous



climate change mitigation projects, the services these ecosystems provide are inherently transient, particularly in the face of mounting climate-related threats. Therefore, special recognition should be placed on the broader significance of maintaining and quantifying forest carbon to address the multifaceted challenges of our changing world.

Wooded lands, which are subcategorized into forests and woodlands, are the largest terrestrial carbon pools.<sup>1</sup>, and thus play a significant role in the global carbon cycle (Xu et al. 2020). Forests usually have a canopy cover greater than 60%, tend to be larger in geographic size, offer more shade, and support more biodiversity than woodlands. Woodlands have varied canopy covers ranging from 5 to 60% but typically have an open canopy structure and sparser tree density, allowing more sunlight to hit the floor, keeping the soil dry and unshaded (OpenAI 2024). The open versus closed canopy structure is an important distinction, as it directly affects the ability to map trees at the individual level. Woodlands also tend to be transitional buffers between forests and more open-grounded regions, such as savannahs and prairies, and host high biodiversity. Wooded Lands act as the largest terrestrial carbon sink<sup>2</sup>, effectively reducing atmospheric carbon and slowing down global warming. Tree carbon content is typically measured as a factor of biomass. Biomass, as dry weight, is approximately 50% carbon, and forests and woodlands comprise 70-90% of terrestrial aboveground and belowground biomass. (Cairns et al., 1997; Houghton et al., 2009). Therefore, measurements of biomass are essential to monitor carbon content properly.

---

<sup>1</sup> Carbon pools are the reservoirs where carbon is stored and released within the Earth's systems. Terrestrial carbon pools include carbon stored in vegetation, soils, and organic matter. There are also atmospheric carbon pools, oceanic carbon pools, and geologic carbon pools.

<sup>2</sup> Carbon sinks are natural or artificial reservoirs that absorb and store CO<sub>2</sub> from the atmosphere, helping to mitigate climate change by reducing atmospheric CO<sub>2</sub> concentrations. This is opposed to carbon sources, which release CO<sub>2</sub> into the atmosphere, contributing to the increase in atmospheric CO<sub>2</sub>.

Obtaining accurate and frequent measurements of biomass is crucial for a multitude of reasons. From a strictly economic standpoint, biomass is the raw material of food, fiber, and fuelwood. The ability to accurately quantify forest productivity is, therefore, crucial to predicting global economic stability. To the ecologist, forest biomass is an important indicator of ecological health as it is related to vegetation structure, which, in turn, influences biodiversity. Forest biomass also has a significant impact on edaphic characteristics, hydrological properties, and fire regimes. Biomass governs the extent and rate of photosynthesis and controls the quantity of carbon released into the atmosphere when ecosystems are disturbed (Houghton et al., 2009). It is crucial to map and assess biomass in order to monitor its impacts on the environment across various scales.

Aboveground biomass (AGB) is specifically of interest to most researchers. While soil organic matter (SOM) holds two to three times more carbon than aboveground biomass, the carbon is physically and chemically protected and not easily oxidized (Davidson & Janssens 2006; Houghton et al. 2009). Conversely, aboveground biomass is in a continuous state of flux due to natural and anthropogenic disturbances, contributing to atmospheric carbon fluxes to a higher magnitude and thus is of far higher interest. The point to emphasize here is that aboveground biomass is ephemeral in nature, and while forests are the largest terrestrial carbon sink, they also have the potential to be one of the largest emitters of carbon when ecosystems are disturbed. Therefore, it is vital that there exists an effective manner to monitor and quantify AGB continually, and not just once and forget thereafter. Forest management plays a significant role in the fight against climate change, yet many complications exist in collecting accurate forest inventory data (Weiskittel et al. 2015; Badgley et al. 2017; Marino et al., 2022). Improved measurement methods are in high demand; thorough, accurate, and frequent measures of

aboveground biomass must be obtained to make effective policy decisions and better understand fluctuations in global atmospheric carbon levels. Accurate monitoring of forest biomass is necessary for carbon stock quantification, forest ecological management systems, and climate change impact assessment.

Current methods for inferring AGB and carbon content have significant limitations; field methods are often too cost-prohibitive, labor-intensive, and time-consuming to be conducted at a large scale, while indirect methods (e.g., remote sensing) tend to lack the required degree of accuracy and precision. Remote sensing techniques offer various approaches for the collection of forest data for biomass estimation. Most remote sensing approaches that rely on orbital or high-altitude aerial imaging systems yield landscape-scale estimates of biomass which, although useful, lack the spatial resolution needed to inform accurate, site-specific evaluations of biomass and do not account for fine-scale spatial heterogeneity (Jones et al. 2020; Lu et al. 2014). The recent development of small unoccupied aerial systems (sUAS) offers a potential alternative means to remotely accumulate the necessary species-specific data for highly accurate AGB estimates.

The use of sUAS for environmental study and management has expanded exponentially in recent years, mainly as a result of technological advances that have given rise to low-cost passive and active remote sensing payloads. For site-specific assessments, sUAS offers comparatively large areal coverage capabilities that surpass those of in-situ data collection. Researchers can now extract exceptionally accurate canopy and height metrics by leveraging the high spatial, spectral, and temporal resolution offered by contemporary sUAS systems. Furthermore, sUAS technology has evolved to become an efficient, cost-effective alternative to other methodologies. Despite the proven effectiveness of sUAS as a powerful research tool, very

little research has investigated the use of variables extracted from high-resolution imagery in field-based allometric equations for aboveground biomass estimation. Consequently, this thesis seeks to explore the efficacy of incorporating remotely sensed variables into species-specific allometric equations as a means of augmenting more traditional methods for estimating aboveground biomass.

Existing allometric equations for a multitude of tree species have been based on three easily obtainable metrics from ground surveys—namely, tree species, height, and diameter and breast height (DBH). While the first two metrics are readily obtainable using conventional image processing techniques, the third is not. As such, this thesis seeks to develop alternative means for measuring DBH via canopy-based estimates. Following Iizuka et al. (2017) and Jones et al. (2020), the working hypothesis of this thesis is that canopy structure can be used to effectively predict DBH for use in existing species-specific allometric models to quantify aboveground biomass.

It should be noted, however, that much of the research on using drones to measure tree metrics and to develop allometric equations has been conducted in conifer forests (e.g., Argomosa et al. 2016; Goodbody et al. 2017; Iizuka et al. 2017; Jing et al. 2012). This approach is relatively untested for hardwoods/broadleaf species, which tend to have more complicated and diverse forms. As such, this study will test the utility of four different canopy metrics for estimating DBH: perimeter, area, volume, and width. This process will require five steps: (i) collect in situ data for the three dominant tree species on the study site for key metrics including DBH, height, and canopy dimensions in order to calibrate the model; (ii) biomass calculation and model calibration via regression analysis to develop linkages between canopy (which can be remotely-sensed) and DBH; (iii) photogrammetry and GIS-based workflow to produce metrics—

including species, height, and canopy dimensions—at the individual tree level; (iv) model calibration via regression analyses with the remotely sensed canopy dimensions and field-based DBH values, and biomass estimation; and (v) accuracy assessment of the remotely sensed data (generated in step (iii)) and biomass estimates (generated in step (iv)).

In summary, while forests and woodlands provide a host of ecosystem services and hold a crucial role in regulating global climate, various challenges exist with contemporary methods for monitoring forest parameters. This thesis aims to develop a procedure to efficiently quantify forest parameters, including aboveground biomass while preserving accuracy. The theory being tested herein is that canopy-based estimates of DBH can provide an accurate quantification of AGB while providing more efficiency and cost-effectiveness than traditional field methods.

## CHAPTER 2

### CONCEPTUAL FRAMEWORK

Contemporary methods of biomass quantification have significant challenges associated with them. The only direct method to weigh biomass is costly in terms of monetary, labor, and time. To obviate these costs, an indirect method was established through tree allometry, or in other words, by establishing relationships between the biophysical parameters of a tree and its aboveground biomass content in order to estimate its AGB. A vast amount of emphasis has been placed on coniferous trees in the past as they are economically significant for timber production in many regions. As a result, allometric relationships for broadleaf tree species are less established in the literature. Nonetheless, in recent years, there has been a growing recognition of the importance of developing allometric equations for a diverse range of tree species. New remote sensing technologies and forest management objectives have placed new value on tree species that may not have traditionally been valued by the timber industry—including the multitrunked or broad-leafed species in this thesis. The following discussion outlines the present state of forest parameter extraction and biomass estimation, including conventional methods as well as novel research, which this thesis tries to emulate.

#### **2.1 Why More Effective Methods of Measurement for AGB are Needed**

A recent study investigated the design of California's prominent forest carbon offsets program, and it demonstrated that California's climate-equivalence claims fall quite short based on directly observable evidence. Badgley et al. (2021) quantify systematic statistical and ecological deficiencies within California's forest offsets protocol, which issues upfront carbon credits to Improved Forest Management (IFM) projects based on flawed calculations of average regional carbon stocks. They pinpoint a prevalent statistical error, referred to as the ecological

fallacy, within the structure of California's forest offsets program—the most significant compliance market currently in operation (Badgley et al. 2021). The ecological fallacy arises when group-level characteristics, such as the average of a distribution, are employed to make inferences about individuals within that group. Weiskittel et al. (2015), in their review of biomass estimation models' limitations, claim that the application of tree biomass models across various spatial scales, ranging from local to international, beyond their original scope can lead to notable errors, reportedly reaching as high as 240%. These points highlight the necessity of analyzing trees at the individual level. The practice of averaging dissimilar tree species across arbitrarily defined geographic regions facilitates, and potentially even encourages, the development of offset projects that assert false carbon credits, primarily through adverse selection (Badgley et al. 2021). Their findings reveal that nearly a third of the credits examined lack genuine climate benefits and instead result from methodological flaws. The key takeaway here is that significant methodological flaws exist within biomass and carbon quantification efforts, leading to serious errors. A potential means for mitigating this error is to look at trees at the individual level rather than applying generalized equations to a sample plot.

## **2.2 How Biomass is Measured**

The “gold standard” for measuring biomass density at a forest sample plot is a labor-intensive and destructive endeavor. The commonly accepted method involves felling a large number of trees of various sizes and geographies representative of the sample area, harvesting all the organic material from each tree, drying it to a constant weight, and then weighing it. This destructive method becomes exponentially more difficult if belowground portions are also accounted for and if the vegetation includes large trees. The sample size and methodology are crucial as small sample sizes will either overestimate or underestimate mean biomass density if

they include or exclude large trees, respectively (Houghton et al. 2009). While this is the only direct method that actually weighs the biomass, it is best reserved for small sample plots where there is uniformity in tree size (e.g., a pine tree plantation). All things considered, the destructive nature, time, costs, and labor involved in this method render it unsuitable for use in large study areas. To counteract these issues, foresters and ecologists have established indirect methods for approximating biomass density. Most commonly, they utilize empirically based allometric equations derived from destructive sampling. These allometric equations are statistical models correlating the actual biomass to certain tree biometrics that can be obtained non-destructively and reasonably easily—namely, diameter at breast height (DBH) and tree height (Maulana et al., 2016)—yielding accurate estimates of aboveground biomass. Furthermore, species-specific allometric equations are favored as trees of distinct species tend to have vastly differing tree architecture and wood density (Ketterings et al., 2001). This indirect approach allows for the calculation of biomass density across a more extensive scale without the limitations of the destructive sampling method. This systematic sampling of aboveground biomass using allometric equations, however, does require in-situ collection of input data, including DBH, height, and taxonomy from representative trees in order to calibrate the allometric equations (Houghton et al., 2009). This technique is also fairly labor intensive and subject to its own limitations, such as the exclusion of trees located in inaccessible areas. Moreover, it is unknown how well these allometric equations perform beyond the “calibration” zone (i.e. when the field data are extrapolated to larger regions), but the accuracy is typically higher for less complex forest structures (Ketterings et al. 2001; Houghton et al., 2009).

Allometric equations can suffer bias introduced from the variables that characterize the site where they were developed. When using allometric equations, caution should therefore be



exercised as topography, soil conditions, forest density, climate, and hydrology are all factors that can vary from site to site and potentially affect allometry between tree biometrics. This variability can, in turn, affect the accuracy of allometric equations (Lu et al., 2014). More importantly, a significant limitation with site-specific equations, in addition to the cost of destructive biomass sampling, is that they are typically based on a small (and oftentimes unrepresentative) sample size (Ngomanda et al., 2014). For instance, Ngomanda et al. 2014 describe situations where, at the time of data collection, a single allometric equation was based on a sampling of more than 30 trees with wide-ranging DBH values.

Based on this author's review of published literature, only one study of similar scope to this thesis has been conducted in California—coincidentally in close proximity to this author's study site—to measure blue oak biomass (Karlik & Chojnacky, 2013). In addition, only one equation exists for interior live oak (Pillsbury & Kirkley, 1984), and there is not a specific equation for California buckeye but rather a plurispecific equation for “mixed hardwoods” (Jenkins et al., 2003). Karlik and Chojnacky's allometric equation is based on 14 blue oaks in the same region as this author's study site, but the sample size may not be large enough to prove statistically significant. Pillsbury and Kirkley's equation for interior live oaks is based on 60 samples obtained throughout their natural range in California, although the equations were developed for use for specific study sites for which detailed descriptions are not provided by the authors. The equations of Jenkin et al. for mixed hardwoods are plurispecific equations intended for general use for any tree that fits that category. When applying allometric equations to estimate biomass, one is consequently confronted with the dilemma of using non-site specific, generalized, or occasionally even plurispecific equations developed from robust but possibly

biased data or using a site-specific equation developed from limited data, and thus characterized by a lower presumed precision of prediction (Ngomanda et al., 2014).

The above discussion implies that careful selection of suitable allometric models for specific tree species is a critical step for conducting biomass studies. When the biomass for a specific study site is the objective, Pillsbury and Kirkley 1984 suggest applying a specific regression model that is matched closely to the site rather than generalized regression models developed for large-scale applications. If such an equation is not available, they recommend applying a range of site-specific equations” (Pillsbury & Kirkley, 1984). This approach yields a series of biomass estimates that both increase the probability that the actual biomass value for the study site will be included and provide a basic estimate of the uncertainty innate in biomass calculations.

While field-based methods generally provide higher degrees of accuracy, remote sensing data offers a means to quantify biomass on a much larger spatial scale. Remote sensing’s distinct advantages for data acquisition, including potentially large aerial coverage and digital format, establish it as the leading data source for large-scale biomass estimation. Remote sensing is defined as a technique that acquires information about an object of interest without being in direct physical contact with it. There are two major categories of remote sensing instrumentation, namely, active systems (sensors emit their own energy source in the direction of a target and measure the backscatter reflected back to the sensor) and passive systems (sensors measure irradiance from the sun reflected off of a target on the Earth’s surface). Variables for modeling aboveground biomass can be acquired through passive optical (e.g., multispectral, hyperspectral, or thermal imagery) or active sensor (e.g., LiDAR or radar) data. With remote sensing, biomass

is commonly modeled through the use of textural information<sup>3</sup> on the vegetation structure or vegetation indices that are correlated with biomass (Kumar & Mutanga 2017). Caution must be exercised when applying such techniques as uncertainties in modeling aboveground biomass using remote sensing data are high due to nuances in vegetation structure, landscape heterogeneity, seasonal variations, and inconsistent data availability, among other factors (Kumar & Mutanga, 2017). While much research has focused on investigating the use of remote sensing in biomass modeling, procedures to choose fitting variables from remote sensing data and to create accurate estimation models are still inadequately understood (Lu et al., 2014). Although remote sensing allows for large-scale biomass estimation, much more research is needed to improve our understanding of appropriate variables and methods.

### **2.3 Aboveground Biomass Estimation Using Remote Sensing Methods**

As stated previously, remote sensing offers a considerable advantage for biomass estimation in that it can provide data over large areas and inaccessible terrain at a fraction of the cost associated with in-situ sampling. Remote sensing data is available at various scales, from local to global, and from a multitude of platforms such as satellites, crewed aircraft, sUAS, and surface-based systems. Passive (optical) and active remote sensing data are readily available for a large portion of the globe, but it is important for the researcher to understand the advantages and limitations of each. own pros and cons. Developing an accurate remote sensing model for estimating biomass requires detailed spatial biomass reference data (Avitabile et al., 2011; Lu et al., 2014) to establish relationships between suitable variables and biomass. Once the

---

<sup>3</sup> Texture describes the patterns or surfaces that can be seen in imagery (e.g., texture helps users discern between smooth surfaces—such as a lake or agricultural field—and rough surfaces—such as a dense forest. Texture can inform users if trees are spaced apart or close together, if they exist in rows, or if they are different kinds of trees. Statistical and mathematical techniques are used to quantify textural information (OpenAI 2024).

prerequisite for accurate biomass reference data is met, there are various ways remote sensing data can be used to estimate biomass.

### Optical Remote Sensing

Optical remote sensing consists of acquiring data about a target of interest through the use of passive imaging systems. This technique involves capturing and recording reflectance values primarily in the visible, infrared, and thermal regions of the electromagnetic spectrum in order to derive information about vegetation structure and vigor. Optical remote sensing offers perhaps the best alternative to in-situ biomass estimation mostly due to its potentially large areal coverage, repeatability, and cost-effectiveness (Kumar & Mutanga, 2017). Optical sensors offer various spatial, spectral, radiometric, and temporal resolutions depending on the type of platform and sensor design. Some of the variables that can be extracted from optical sensors for use in biomass estimation include vegetation indices,<sup>4</sup> image transform algorithms, texture measures, and spectral mixture analysis (Lu et al., 2014). Vegetation indices have been correlated with biomass, but the relationships vary with forest complexity and soil properties. There are methods for extracting texture from imagery, but textural data alone is a poor indicator of biomass, especially in simple forest stand structures. However, combining texture with spectral response (e.g., vegetation index or spectral signature) strengthens biomass estimation compared to using only one or the other (Lu et al., 2014).

While optical remote sensing data have been the primary source for biomass modeling, prior studies by other researchers have revealed that data saturation, particularly in forested areas

---

<sup>4</sup> A vegetation index is a numerical measure that quantifies some vegetation parameter (e.g., plant biomass and plant health) derived from a multispectral image. The index is calculated from spectral bands that are sensitive to vegetation characteristics such as vigor, moisture content, or biomass. They are used to enhance sensitivity to vegetation characteristics and reduce confounding factors such as soil background reflectance or atmospheric effects (OpenAI 2024).

with above-average densities of biomass, is one of the critical issues causing weak biomass estimation performance (Lu et al. 2014). Spectral-based variables also tend to be unpredictable and affected by outside factors such as atmospheric conditions, edaphic (soil-related) characteristics, vegetation phenology, and vigor (Lu et al., 2014). The traits of vegetation and the intricate biophysical conditions of the surrounding environment affect spectral signatures. Consequently, models that estimate biomass based on spectral variables cannot be reliably transferred to widely separated study sites. Optical sensors are also affected by atmospheric conditions such as scattering, the presence of clouds, and aerosols (mostly soot and salt crystals), which negatively impact the acquisition of images, particularly in tropical regions. Nonetheless, optical remote sensing data excel at revealing horizontal vegetation structure (e.g., vegetation type and canopy dimensions). On the other hand, some optical sensors (particularly those fitted to orbital platforms) are not well-suited for use in the extraction of vertical vegetation features such as height, which is a crucial parameter for biomass estimation. It should be noted that some optical sensors provide stereo-viewing capability, which allows for the acquisition of vertical data and improves the accuracy of biomass estimates.

### Radar Remote Sensing

RADAR (Radio Detection and Ranging) has recently garnered interest for biomass modeling mainly due to its ability to accurately model vegetation structural attributes in practically any prevailing weather condition. In particular, Synthetic Aperture Radar (SAR) is gaining prominence for its potential to accurately survey aboveground biomass by leveraging its ability to penetrate cloud cover and forest canopy and sensitivity to water content in vegetation (Lu et al., 2014). Nonetheless, achieving data saturation is also an issue with radar methods when backscattering values are employed to model biomass. One alternative used to address the data

saturation problem is the use of Interferometry Synthetic Aperture Radar (InSAR). Lu et al. define InSAR as “a technique in which the coherence of data is collected over a short time increment by two identical instruments.” The referenced authors also report that InSAR can increase the saturation range to a certain degree and thus improve the height-based biomass estimation. Despite its distinct advantages, InSAR data has been shown to be highly dependent on site conditions such as temperature, wind speed, and humidity, and variations in these conditions can negatively impact the accuracy of biomass estimation. Moreover, radar data is not suitable for differentiating vegetation *types*, a limitation that further reduces the accuracy of biomass estimates.

### LiDAR Remote Sensing

LiDAR (Light Detection and Ranging) remote sensing is a comparatively recent technology that is gathering increasing attention for biomass modeling. Although similar in concept to RADAR, LiDAR systems use laser light rather than radio signals to generate three-dimensional models of terrain and vegetation structure. Much research has shown a strong link between LiDAR-based vegetation parameters and aboveground biomass. With aerial LiDAR, measurements can be obtained for either individual trees or entire forest stands (Chen, 2013). The methodology for extracting metrics for individual trees entails delineating individual tree features such as treetop, crown radius, or crown perimeter. LiDAR’s ability to resolve the vertical distribution of forest canopies as well as the terrain surface below enables researchers to generate highly detailed models of vegetation structure and thus illustrates great potential for biomass quantification (Lefsky et al., 2002). Area-based methods are now widely used to generate statistical metrics derived from the LiDAR point cloud or canopy height model at the plot or stand level and employ the models across the entire study site (Chen, 2013; Lu et al.,

2014). The vast majority of LiDAR metrics can be created from either point clouds or canopy height models. Although LiDAR's ability to extract both horizontal and vertical canopy structure makes it extremely useful for biomass estimation, LiDAR as a remote sensing tool does come with its own limitations. For example, modeling individual trees demands high point cloud density and thereby requires more storage space and processing time. In addition, the 3D distribution of a tree's laser point cloud can fluctuate due to changes in point density, scan angle, and footprint size, all of which are dependent upon individual sensor design and flight parameters used for data acquisition (Lu et al., 2014). LiDAR payloads are also more costly and heavier compared to optical sensor payloads, and the extra weight translates to less efficient data acquisition when collecting data with sUAS.

#### Structure from Motion (SfM)

A 2016 study by Wallace et al. investigated the potential application of sUAS aerial imaging to quantify structural properties of forests by comparing two different remote sensing techniques: aerial laser scanning (ALS)<sup>5</sup> and structure from motion (SfM). SfM is a photogrammetric technique that enables the modeling of three-dimensional surfaces using overlapping sequences of two-dimensional aerial and/or terrestrial images. As part of their study, the authors tested and compared the ability of ALS and SfM to accurately reconstruct a 30m x 50m scene consisting of a dry sclerophyll eucalyptus forest with spatially varying densities of canopy cover. Their results indicate that both techniques are suitable for acquiring accurate data on terrain and forest attributes for areas of relatively low canopy closure; however, ALS outperforms SfM in capturing the terrain surface in areas where canopies are denser. Due to the

---

<sup>5</sup> ALS refers to a LiDAR payload mounted on an aerial platform for the acquisition of data. This is opposed to Terrestrial Laser Scanning (TLS) where a LiDAR payload is mounted on a ground-based vehicle or pole for the acquisition of data.

ability of ALS to penetrate dense vegetation and model vegetation and terrain surfaces in areas that are invisible to conventional aerial imaging, ALS scans produce better point clouds and, in turn, more accurate digital elevation models and tree height and canopy data.

Another study conducted in 2017 by Mlambo et al. aimed to assess whether SfM from sUAS could serve as a cost-effective method for forest monitoring in developing countries, particularly within the framework of Reducing Emissions from Deforestation and Forest Degradation (REDD+) activities. That project assessed the horizontal and vertical accuracy of SfM in measuring individual tree heights. Aerial imagery was acquired for two sample sites and the derived SfM digital surface models were compared to LiDAR-generated-digital surface models and surface models at the first site, and ground measured tree heights at the second. The results demonstrated a robust correlation between the SfM and LiDAR digital surface models ( $R^2 = 0.89$ ) and canopy height models ( $R^2 = 0.75$ ) at the first site. Conversely, at the second site, a weak correlation was observed between SfM tree heights and ground-measured heights ( $R^2 = 0.19$ ). The suboptimal performance at the second site was attributed to the closed canopy structure of the forest plot, limiting the generation of below-canopy ground points by SfM. Without sufficient ground points, it is challenging to interpolate the ground surface from aerial imagery, and, as a result, the accuracy of the SfM-derived tree heights suffers. Additionally, the study evaluated the efficacy of sUAS surveying methods for plot-level forest monitoring. Despite its limitations in closed canopies, SfM modeling using sUAS imagery can still offer a cost-effective solution in developing countries where forests have sparse canopy cover (<50%), enabling effective capture of individual tree crowns and ground surfaces through SfM photogrammetry.



A recent 2020 study by Xu et al. examined the use of SfM-derived point clouds and multispectral imagery to classify tree species in a subtropical forest. The authors of that study used SfM technology to generate a point cloud and then subsequently classified the dominant tree species in a heterogeneous forest using a mix of spectral data and structural data. They implemented a multi-resolution segmentation (MRS) algorithm based on edge detection with a segmented image derived from a mosaic dataset consisting of a canopy height model (CHM) and an RGB orthomosaic to delineate individual tree crowns (ITCs). Their research illustrated the potential of SfM point clouds to extract 3D vegetation structure and a useful methodology to distinguish tree species. Their research indicates that SfM point clouds are comparable to LiDAR-derived point clouds in forests with an open canopy structure. They can be used in conjunction with optical multispectral sensors to acquire spectral-based variables and vegetation structural characteristics.

#### Integration of Multisource Data

Optical sensors, radar, and LiDAR all have their advantages and disadvantages; however, assimilation of data acquired using two or more of these technologies can effectively reduce the negative effects of these limitations and enhance the accuracy of biomass estimates. Lu et al. (2014) contend that effective integration of sensor types is necessary to improve biomass estimation. Combining LiDAR data with optical multispectral data yields a dataset with both structural and spectral metrics, both of which are known to increase biomass estimation performance. On the other hand, prior research has demonstrated mixed results when integrating LiDAR with optical data (Lu et al., 2014). Another method that fuses multiple types of data uses spectral metrics to distinguish vegetation types, a useful variable for allometric models. Chen et al. (2012) implemented this approach and integrated optical multispectral and LiDAR data for

modeling biomass in California. Their findings suggested that the availability of information on vegetation type can drastically increase the estimation accuracy of biomass.

### Linking Tree Canopy to DBH

While there exists an emerging trend toward utilizing sUAS to collect data for various forestry-related analyses, the relationships between biophysical parameters such as tree canopy—which can be readily obtained through sUAS imaging—and DBH have seldom been described. Research conducted by Izuka et al. (2017) aimed to evaluate the utilization of photogrammetry for estimation of forest parameters. Specifically, they wanted to test the reliability of using canopy dimensions to estimate DBH. Their analysis revealed that canopy metrics are highly correlated with individual tree DBH, thus suggesting that sUAS imagery can indeed be used to efficiently inventory forests and effectively monitor aboveground biomass.

This thesis investigated DBH from canopy metrics that could be easily obtained from sUAS image acquisition missions. This approach stemmed from literature suggesting that the growth of DBH could be influenced by various factors beyond just tree height (Izuka et al., 2017), a notion corroborated by observations made in the field. Existing literature suggests that the trajectory of DBH growth may vary depending on factors such as foliage density, light exposure, wind patterns, and water availability, all of which contribute to tree architecture (Izuka et al., 2017). Thus, instead of focusing on tree height, canopy structure was the main focus for the estimation of DBH.

### Remote-Sensing-Based Allometric Modeling

Although LiDAR and SfM point clouds provide 3D data pertaining to vegetation structure, it is quite challenging to derive detailed information about dimensions *under* the canopy (such as the diameter of the trunk) from remotely sensed data. For this reason, remotely

sensed data has traditionally not been considered suitable for use in biomass modeling with allometric equations, which rely on accurate data about trunk diameter. Nevertheless, a recent 2021 study by Jones et al. demonstrates the potential for incorporating remote sensing in allometric modeling. In their study, the authors demonstrated proof-of-concept for utilizing variables obtained from sUAS imagery to estimate aboveground biomass in a mangrove forest. Their research confirmed that the diameter of the tree trunk is the best predictor of biomass, and other biometrics, such as tree height and canopy area, have poor relationships with biomass. Recognizing the fact that trunk diameter cannot be determined reliably from sUAS imagery, they instead ran their regression models based on known correlations between remotely sensed canopy metrics and DBH. They used the relationships between canopy and trunk diameter to predict DBH, thereby allowing them to predict aboveground biomass using the predicted DBH values. One critical element of the referenced study is that the authors had a very small sample size to work with ( $n = 10$ ), thus lowering their ability to clearly establish the link between canopy area, tree height, and diameter metrics (Jones et al., 2020). Nonetheless, their study illustrates the potential for employing sUAS imagery to develop three-dimensional models of tree structure and acquire biometric measurements to estimate aboveground biomass (AGB) and carbon.

The discussion above provides an overview of the current state of biomass estimation, the different procedures used, the pros and cons of each method, and the need for an improved methodology. The literature indicates that canopy has a strong link to DBH and can thus be used to measure AGB indirectly. The canopy-DBH relationship may very well be unique for different tree species, especially with coniferous and broadleaved trees (and potentially with softwoods and hardwoods). This research will, therefore, test the relationships between canopy and DBH for each tree species. The objective of this research is to produce estimates of AGB using sUAS

imagery in an attempt to find a more accurate and efficient site-based method of AGB estimation compared to current methods. This research will reveal which canopy biometric is the best predictor of DBH for broadleaved trees in our study area.

The use of passive optical sensors as payloads on sUAS for environmental study and management has expanded exponentially in recent years. The advantages of these types of low-altitude remote sensing systems are clear; they allow for far greater coverage in less time than in-situ data collection, they can acquire highly accurate canopy and height metrics as derived from imagery and point cloud data using SfM technology, and they are relatively inexpensive, less data-intensive and allow for more efficient data collection compared to LiDAR. In the final analysis, they are more efficient, less labor intensive, and more cost-effective than other methods. Using sUAS-derived tree biometrics to predict DBH combined with the deployment of allometric equations demonstrates potential to be a powerful tool for biomass estimation. Consequently, this thesis proposes a procedure wherein forest inventory techniques and remotely sensed imagery are combined as a means to quantify aboveground biomass and carbon for the blue oak woodland on a study site described in Section 3.1 of this thesis.

## CHAPTER 3

### METHODS AND APPROACH

This project aims to develop a remotely sensed procedure for determining ABG for a representative California Oak woodland landscape. This requires five steps (see Figure 1): (i) collect in situ data for the three dominant tree species on the study site for key metrics, including DBH, height, and canopy dimensions in order to calibrate the model; (ii) biomass calculation and model calibration via regression analysis to develop linkages between canopy (which can be remotely-sensed) and DBH; (iii) photogrammetry and GIS-based workflow to produce metrics—including species, height, and canopy dimensions—at the individual tree level; (iv) model calibration via regression analyses with the remotely sensed canopy dimensions and field-based DBH values, and biomass estimation; and (v) accuracy assessment of the remotely sensed data (generated in step (iii)) and biomass estimates (generated in step (iv)).

This research consisted of acquiring true-color and multispectral imagery using a fixed-wing sUAS in conjunction with field data, supervised digital image classifications, and image segmentation methods to determine whether these remote sensing methods can provide a basis for accurate assessments of dominant tree species and aboveground biomass. Initially, data were collected in the field, and then statistical analysis and biomass calculation were performed with the field data. Following field data collection, the sUAS imagery were collected and digitally processed using Structure from Motion (SfM) software to generate a SfM point cloud and both a true-color and multispectral orthomosaic. Next, supervised classification via object-based image analysis (OBIA) was used to delineate the dominant tree species. Finally, the biophysical tree data generated from the remotely sensed imagery were compared with the field data and used to generate estimates of aboveground biomass.

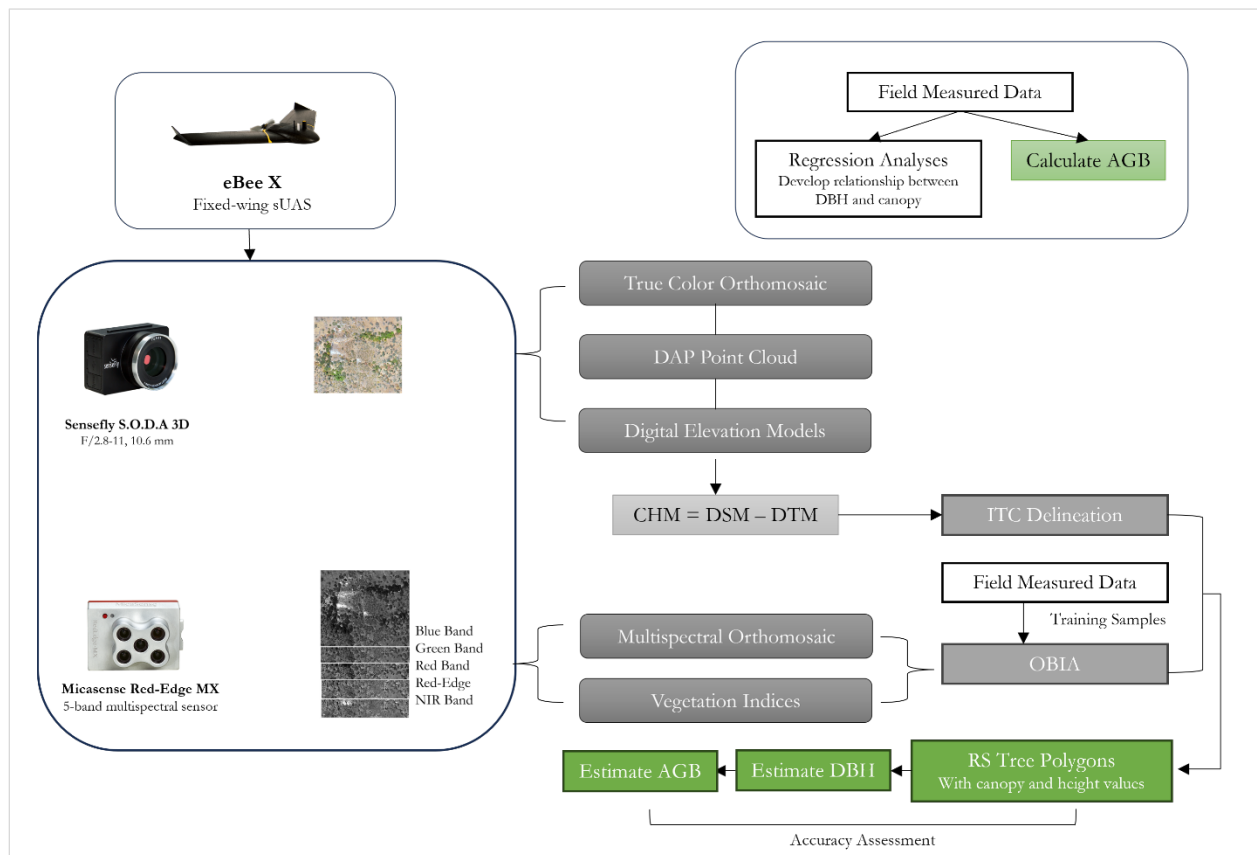
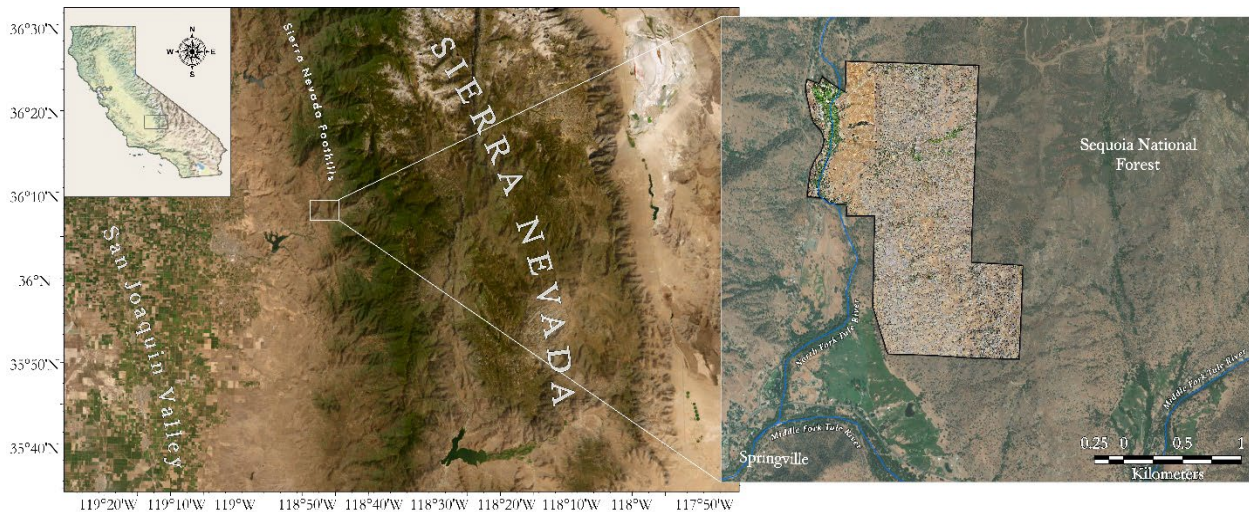


Figure 1: The general workflow employed in this thesis.

### 3.1 Study Site

This research was conducted at River Ridge Ranch, a 722-acre former cattle ranch located in the western foothills of the Sierra Nevada mountains of central California (see Figure 2). The ranch is situated along the easternmost perimeter of the San Joaquin Valley, which, in turn, comprises the southern portion of California's Central Valley. The climate in this area is characterized by hot, dry summers and cool, rainy winters. Significant winter snowfall is uncommon, although a light dusting occurs occasionally with the passage of cold Pacific winter storms. The region has an average annual precipitation of 283 mm and an average annual temperature of 23 °C. The average annual low temperature at this relatively low-elevation site is 2.3 °C with an average summer daytime high of 36.8 °C (1961-1990). The River Ridge Ranch property is characterized by a highly varied topography, locally high relief, and elevations that range from 311 meters to 867 meters above the WGS 84 ellipsoid.



**Figure 2:** Location of study site, River Ridge Ranch, a former cattle ranch and current working reserve near Springville, CA in the Sierra Nevada Foothills. The map images are basemaps from ArcGIS Pro (ver. 3.1.2) along with an orthomosaic stitched together from our drone imagery in Pix4D.

This landscape of River Ridge Ranch is best described as a blue oak woodland dominated by three broadleaved hardwood tree species. The ranch comprises three distinguishable habitat types: riparian, pasture, and hillside. Owing to the availability of surface water throughout the year, the riparian corridor produces a much higher abundance and diversity of trees and tree species than the hillside area. The pasture was cleared of trees during the original settlement period (ca. the late 1800s) to make sufficient land for grazing, and for this reason, is mostly devoid of trees. Given the relative absence of trees in the flat-lying pasture, this research focuses on the sloping portions of the ranch where there is a sparse to moderately dense distribution of trees. The hillside has an overall west-facing aspect with heterogeneous microtopography. There are also several drainage basins and small, ephemeral tributary streams which produce a more clustered distribution of trees than the open canopy seen throughout the remainder of the ranch. Appendix A shows images representative of the general landscape of the ranch. The blue oak woodland provides a unique research opportunity as multitrunked trees of the types common to River Ridge Ranch have largely been neglected in the literature, at least at the individual tree level.



### 3.2. Step I: Field Measurements

This study focuses on the three dominant species that populate the sloping portions of the ranch. These include blue oak (*Quercus douglasii*), interior live oak (*Quercus wislizeni*), and buckeye (*Aesculus californica*). A variety of biophysical parameters were recorded as part of the ground survey. Positional data were collected using sub-meter-accuracy Eos Arrow 100 GNSS receivers and were used to map the drip line of tree crowns in-situ. Diameter tapes were used to collect the DBH for sampled trees. In instances where trees had multiple trunks, the DBH was initially collected for each trunk. This technique was later modified such that the DBH was calculated by taking the square root of the sum of all the squared DBH measurements. Laser rangefinders (TruePulse 360R) were used to measure tree height using the sine method in which three distance measurements are taken using the rangefinder —namely, where the tree meets the ground, at eye level, and at the top of the tree. The angles formed from eye level to the top and bottom of the tree and the distances to these points were used to calculate tree height (see Figure 3). All tree measurements and positional data were recorded in real-time using a web map that was accessed via a mobile GIS application (Esri Field Maps). Figure 4 shows the distribution of collected trees on the ranch, as well as a false-color composite and DTM to illustrate the vegetation and terrain conditions.

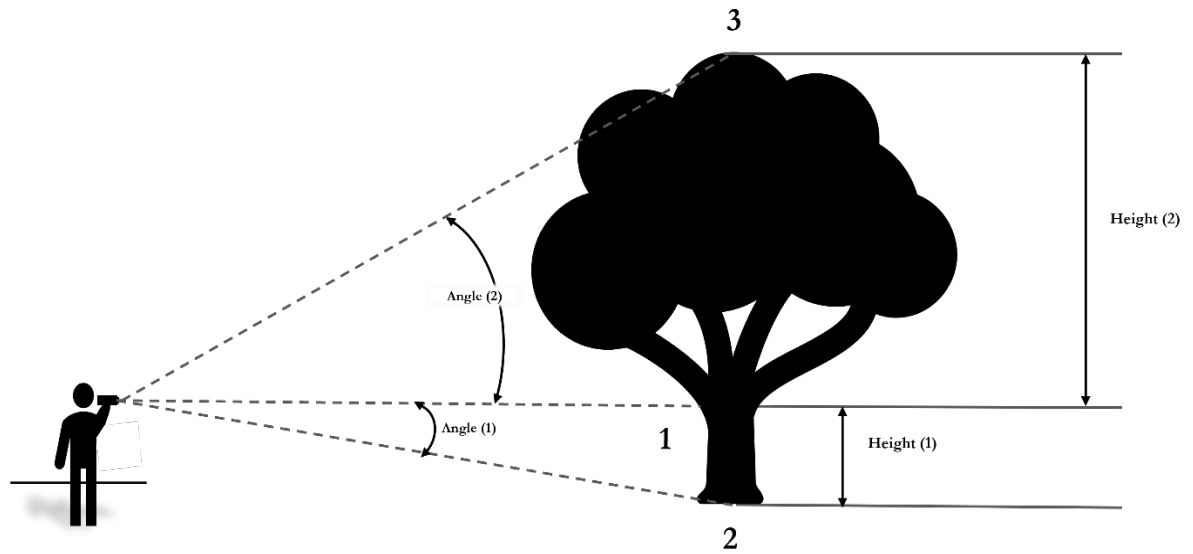


Figure 3: Depiction of the sine method of measuring tree height.

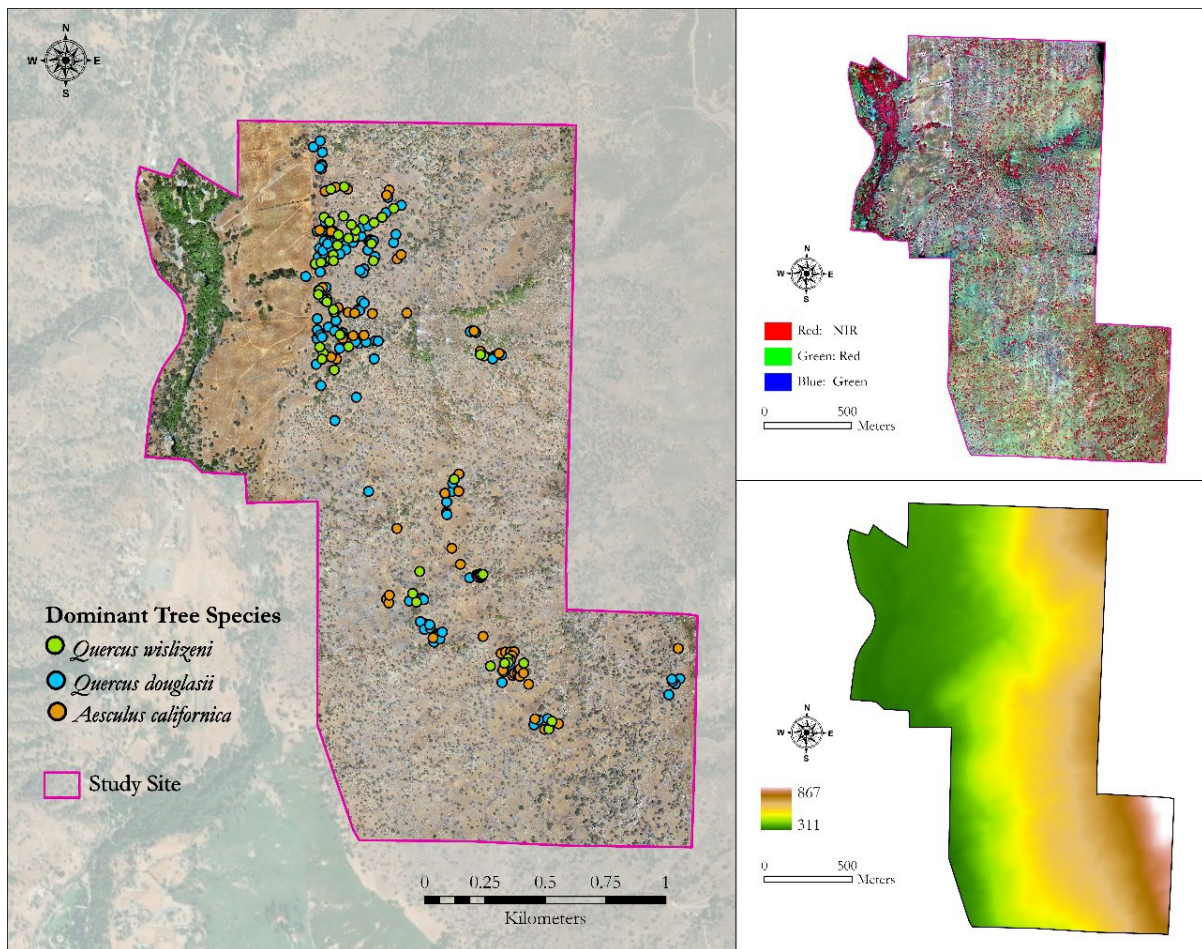


Figure 4: Overview of River Ridge Ranch with the locations of the field collected samples, false color composite (NIR, red, and green), and DTM.

### 3.3 Step II: Biomass Calculation and Model Calibration via Regression Analyses

#### AGB Ground Truth Data and Estimates

Species-specific allometric equations were used to calculate the observed aboveground biomass values for the trees sampled during the ground surveys. The biophysical parameters acquired for each tree, typically DBH and tree height, were plugged into the species-specific allometric equations to quantify AGB, thereby yielding the observed values. Next, the DBH estimates calculated from the different canopy dimensions from both the field and remotely sensed data were plugged into the species-specific allometric equations and compared to the observed values. Table 1 shows the allometric equations used for each tree species.

Table 1: Species-specific allometric equations

	Blue Oak	Live Oak	Buckeye
Species Specific Allometric Equation for Calculating AGB	$AGB = (.0000697541 * (DBH^{2.33089}) \times (HT^{0.461})^{*755}$	$AGB = (.0000446992 * (DBH^{2.31958}) \times (HT^{0.62528})^{*700}$	$AGB = \exp(-2.48 + 2.4835 \times \ln(DBH))$
Reference	<i>Pillsbury &amp; Kirkley (1984)</i>	<i>Pillsbury &amp; Kirkley (1984)</i>	<i>Jenkins et al (2004)</i>

#### Statistical Analysis

Statistical analysis was conducted in both Microsoft Excel (Microsoft, 2023) and SPSS Statistics software (IBM, 2023). Excel was used to sort the data alphabetically by tree species and calculate summary statistics. Simple regression analyses were performed for four separate metrics of tree canopy—canopy perimeter, crown area, crown width, and canopy area multiplied by tree height (a proxy for canopy volume represented as CA\*H)—and tree trunk diameter at breast height (DBH) for each tree species. SPSS was used to perform multiple regression analyses using three different modeling methods (forward, backward, and enter). These analyses were performed on the field data to establish relationships between canopy and DBH to investigate the usefulness of this method.

### **3.4 Step III: Photogrammetry and GIS-based Extraction of Tree Parameters**

#### Remote Sensing Data Collection

True color and multispectral imagery were required in order to obtain the critical parameters for use in the model proposed in this thesis—species information and canopy. In June of 2022, this research team acquired aerial imagery of the entirety of River Ridge Ranch using a SenseFly (now AgEagle Aerial Systems) eBee X fixed-wing sUAS. The initial imaging mission was performed on June 14, 2022, and included the collection of over 4,500 images using a Sensefly SODA 3D true color (RGB) 20-megapixel camera. The camera was programmed to simultaneously collect both vertical (at-nadir) as well as low-angle (28°) oblique images to enhance the SFM point cloud generation. On June 21, 2022, multispectral imageries were collected using a MicaSense RedEdge-MX five-band sensor capable of capturing imagery in the three visible bands (red, green, and blue) and two near-infrared (NIR) bands. This camera was also flown as a payload aboard the senseFly eBee X platform. Geolocation of all RGB and multispectral imagery was augmented using real-time kinematic (RTK) differential corrections provided by a SenseFly GeoBase GNSS base station. SenseFly’s proprietary eMotion 3 mission planning and flight management software was used to plan and conduct each flight. eMotion functions as a fully autonomous desktop flight monitoring system that continuously streams in-flight data produced by the eBee’s onboard autopilot, GPS, inertial measurement unit (IMU), and camera payload. Both the true color and multispectral imaging missions were flown in four blocks to cover the extent of the study site. All imagery was collected between 11 am and 2 pm local time with optimal weather conditions to minimize distortion from shadows and atmospheric effects. The parameters of the sUAS flights are shown in Table 2 below.

**Table 2:** Imagery acquisition parameters

Parameters	MicaSense RedEdge-MX	SenseFly SODA 3D
Flight height (m)	121	121
Ground speed (m/s)	30	30
Forward overlap (%)	80	80
Lateral overlap (%)	80	80
Spectral bands	Blue, Green, Red, Red-edge, and Near-infrared	Blue, Green, and Red
Ground sample distance (m)	0.1	0.1
Image format	16-bit TIFF (Tagged Image File Format)	16-bit TIFF

### Image Processing

Both multispectral and true-color data were digitally processed using Pix4D Professional photogrammetry software (Pix4D SA, 2023). The Pix4D processing algorithm is based on structure from motion (SfM), a photogrammetric technique that allows the reconstruction of three-dimensional landform structure from a series of overlapping two-dimensional images. The images' metadata (RTK-corrected GNSS location and platform orientation from the onboard IMU) are used to calculate the camera positions and orientations for each image to estimate the 3D structure of the scene. The output products from the photogrammetric processing included high-resolution orthomosaics for the entire River Ridge Ranch site, as well as 3D point cloud data and digital elevation products (including digital surface models and digital terrain models). The true color and multispectral imagery processing parameters are outlined in Appendix B and C, respectively.

3,570 images with an average GSD of 4.12 cm were fused together to generate the true color orthomosaic with an X, Y, and Z geolocation RMSE of 1.6 cm, 1.8, and 1.7 cm, respectively. All 3570 images were calibrated, and there was a median of 10450.6 matches per calibrated image and a density of 48.79 3D densified points per cubic meter. 25,825 images (5,165 per reflectance band) were acquired over the course of the multispectral image acquisition

mission. The images were used to generate five individual orthomosaics for each reflectance band with an X, Y, and Z geolocation RMSE of 2.3 cm, 2.1 cm, and 1.6 cm, respectively. 25,773 out of the 25,825 were calibrated (99%), and there was a median of 2265.99 matches per calibrated image and an average density of 10.72 3D densified points per cubic meter.

<b>True Color (RGB)</b>	
<b>Initial Processing Options</b>	
<b>System Information</b>	
Hardware	CPU: AMD Ryzen Threadripper 3970X32-Core Processor RAM: 256GB GPU: NVIDIA GeForce RTX3070 (Driver: 30.0.14.7212)
Operating System	Windows 10 Education, 64-bit
<b>Coordinate Systems</b>	
Image Coordinate System	WGS84
Output Coordinate System	WGS84 / UTMzone 11N
<b>Processing Options</b>	
Detected Template	SODA 3D Oak Savanna
Keypoints Image Scale	Full, Image Scale: 1
Advanced: Matching Image Pairs	Aerial Grid or Corridor
Advanced: Matching Strategy	Use Geometrically Verified Matching: yes
Advanced: Keypoint Extraction	Targeted Number of Keypoints: Custom, Number of Keypoints: 50000
Advanced: Calibration	Calibration Method: Geolocation Based Internal Parameters; Optimization: All; External Parameters Optimization: All; Rematch: Custom, yes
<b>Point Cloud Densification</b>	
<b>Processing Options</b>	
Image Scale	multiscale, 1 (Original image size, Slow)
Point Density	Optimal
Minimum Number of Matches	2
3D Textured Mesh Generation	no
<b>DSM, Orthomosaic, and Index Details</b>	
<b>Processing Options</b>	
DSM and Orthomosaic Resolution	10 [cm/pixel]
DSM Filters	Noise Filtering: yes Surface Smoothing: yes, Type: Medium
Raster DSM	Generated: yes; Method: Triangulation; Merge Tiles: yes
Orthomosaic	Generated: yes; Merge Tiles: yes; GeoTIFF Without Transparency: yes Google Maps Tiles and KML: no
Raster DTM	Generated: yes; Merge Tiles: yes; DTM Resolution: 10 [cm/pixel]

Figure 5: Pix4D parameters used for processing the true color imagery.

<b>Multispectral</b>	
<b>Initial Processing Options</b>	
<b>System Information</b>	
Hardware	CPU: AMD Ryzen Threadripper 3970X 32-Core Processor RAM: 256GB GPU: NVIDIA GeForce RTX 3070 (Driver: 30.0.14.7212)
Operating System	Windows 10 Education, 64-bit
<b>Coordinate Systems</b>	
Image Coordinate System	WGS84
Output Coordinate System	WGS84 / UTM zone 11N
<b>Processing Options</b>	
Detected Template	RedEdgeMX 5Band
Keypoints Image Scale	Full, Image Scale: 2
Advanced: Matching Image Pairs	Aerial Grid or Corridor
Advanced: Matching Strategy	Use Geometrically Verified Matching: yes
Advanced: Keypoint Extraction	Targeted Number of Keypoints: Custom, Number of Keypoints: 10000
Advanced: Calibration	Calibration Method: Geolocation Based; Internal Parameters Optimization: All; External Parameters Optimization: All; Rematch: Auto, no
Rig «RedEdge-M» processing	optimize relative rotation using a subset of secondary cameras
<b>Point Cloud Densification</b>	
<b>Processing Options</b>	
Image Scale	multiscale, 1 (Original image size, Slow)
Point Density	Optimal
Minimum Number of Matches	3
3D Textured Mesh Generation	no
Advanced: Image Groups	Blue, Green, Red, NIR, Red-edge
<b>DSM, Orthomosaic, and Index Details</b>	
<b>Processing Options</b>	
DSM and Orthomosaic Resolution	10 [cm/pixel]
DSM Filters	Noise Filtering: no Surface Smoothing: no
Orthomosaic	Generated: yes; Merge Tiles: yes; GeoTIFF Without Transparency: yes Google Maps Tiles and KML: no
Radiometric calibration with reflectance target	yes
Index Calculator: Reflectance Map	Generated: yes; Resolution: 1 x GSD (11.2 [cm/pixel]); Merge Tiles: yes
Index Calculator: Indices	NDVI

Figure 6: Pix4D parameters used for processing the 5-band multispectral imagery.

## OBIA Species Classification

Object-based image analysis (OBIA) is a technique used in remote sensing and digital image processing to extract information from images. With OBIA, rather than analyzing individual pixels, the analysis is performed on image objects or segments, which are groups of pixels that share similar characteristics, such as color, texture, or shape. This is achieved by first segmenting the image. Segmentation is the process of dividing an image into homogeneous regions or segments based on specific criteria such as spectral properties, texture, or contextual information (OpenAI, 2024). Next, training samples are provided or generated to train the algorithm to extract features. Then, based on the extracted features, the segments are classified into different classes or categories using machine learning algorithms such as decision trees, support vector machines, or neural networks.

The multispectral orthomosaic was used as an input for OBIA to classify the tree species on the ranch. This analysis required several prerequisite steps, including: (i) the five single-band images generated by the multispectral camera were layer-stacked using the image processing toolset in the ArcGIS Pro GIS software (Esri, 2023) to create a single five-band multispectral composite; (ii) the multispectral composite, along with the canopy height model (CHM)<sup>6</sup> and a soil-adjusted vegetation index (SAVI)<sup>7</sup> were aggregated into a mosaic dataset; (iii) a segmented image was generated from the mosaic dataset by using the segment mean shift tool. The segment mean shift tool has customizable parameters that affect the segmentation algorithm, including the spatial and spectral detail where values range from 1.0 to 20.0. Higher values put more weight on

---

<sup>6</sup> A canopy height model (CHM) is the product of subtracting a digital terrain model (DTM) from a digital surface model (DSM). Any positive values in the CHM represent non-ground features such as trees or artificial structures.

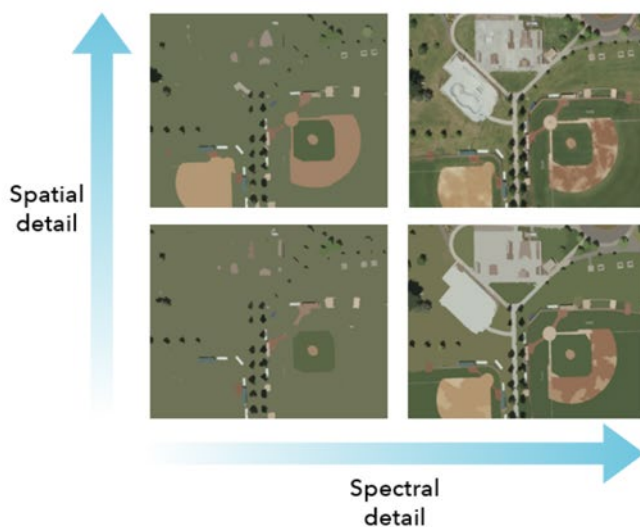
<sup>7</sup> A soil-adjusted vegetation index (SAVI) is a vegetation index commonly used in remote sensing and image analysis to assess vegetation health and density while compensating for variations in soil brightness, especially in areas with bright soil or sparse vegetation cover.



tiny nuances within the image (Figure 7 illustrates different parameter values' effects on the segmentation results). This tool can also adjust the minimum segment size in pixels, where segments smaller than the user's defined size are merged with the closest fitting neighbor. The following parameters were used for the segment mean shift tool: spatial detail: 14; spectral detail: 18; minimum pixel size: 50.

### Adjusting segmentation results

Segmentation can greatly affect the quality of the classification results. When creating your segmented raster, you should consider the settings used to create the segments. The spatial detail and spectral detail can be modified independently, with values between 1 and 20. Properly segmented rasters are a balance of spectral and spatial detail. The segments can be very different, depending on the settings. The segment size based on pixels can also be modified to select larger or smaller segments.



*This segmentation parameter graph depicts how altering the spatial and spectral detail affects how recognizable the features are.*

Figure 7: Illustrates the impacts of parameter choices on segmentation results (ESRI 2024).

The Image Classification Wizard in ArcGIS Pro was then utilized to run a supervised classification of the segmented image that was produced via OBIA. The first step within the classification wizard is to configure the model. In this step, the user chooses the classification method, selects any input datasets to help with classification, and also optionally provides a classification schema. The next step in the classification wizard involves using a training sample manager, which allows the user to use a pre-defined set of classification training samples or to create new training samples by on-screen digitizing. Roughly 30 to 40 training samples were

created for each of the three dominant tree species as well as for shrubs, shadows, rocks, and soil. The classification schema was generated from the provided training samples. The next step in the classification wizard is to select the type of classification method to use. Choices include ISO Cluster, K-Nearest Neighbor, Maximum likelihood, Random trees, or Support vector machine. This research employed the support vector machine (SVM) classifier, a sophisticated machine-learning classification technique capable of handling segmented raster inputs and standard images. This method was chosen because it exhibits reduced sensitivity to noise, correlated bands, and imbalances in the number or size of training samples across different classes compared to other available methods. The output generated from this classification method is a discrete raster dataset where pixels are aggregated into spectrally similar objects based on the defined number of classes from the provided training samples. The raster dataset included classes for the three target tree species, shrubs, shadows, rocks, and a catch-all class for other land cover that does not fit into one of these categories. This raster dataset was filtered to include only the target tree species and converted to vector features (polygons), which describe the boundaries of the trees and contain species information as attributes.

#### ITC Generation

An individual tree crown delineation method was attempted to separate trees out at the individual level. The method employed is a GIS-based model that utilizes a canopy height model as the primary input from which local maxima (i.e., the highest point on a tree crown) are determined by identifying the maximum raster value within a 10m x 10m cell. These local maxima values are interpreted as treetops representing individual trees. Theissen polygons are then generated based on these assumptions to define the extent of the canopy. This method was adapted from research conducted by Argomosa et al. (2016), but while they developed their

model in a coniferous plantation, the research in this thesis takes place in a nonuniform stand of multitrunked deciduous trees in a mountainous region. They use negative curvature values calculated from their CHM to represent the outside of their tree crowns and, in conjunction with the Theissen polygons, generate individual tree crowns (ITCs). However, oak tree canopy shapes are more complex, making it difficult to calculate true treetops and negative curvature values. Thus, a simplified approach was employed where the Theissen polygons were used to split the classified tree polygons from the OBIA workflow where multiple trees overlapped. While this modified approach is overly simplistic, it is easy to perform and results in more accurate polygons than the ones generated from the species classification alone where canopies overlap.

#### Estimating and Analyzing Tree Parameters

The Theissen polygons were used to split the polygons from the OBIA workflow to represent individual trees. The resulting ITCs had species information, and canopy perimeter and area were automatically calculated from the ITCs' geometry. Canopy width was calculated by measuring the width of each polygon in two cardinal directions and computing the average of both. The canopy area was multiplied by tree height ( $CA * H$ ) to give an approximate measure of volume. Trees less than 3 m in height and all shrubs were not considered in the ground sample and were thus filtered out of the CHM. The local maxima in 10 m x 10 m cells from the CHM were converted from raster data to points and then spatially joined to the remotely sensed ITCs to represent tree heights for individual trees. The in-situ tree polygons were overlaid on the remotely sensed tree polygons, and the data from the remotely sensed trees with the largest overlap with the in-situ data were spatially joined to the in-situ attribute table. All the biophysical parameters of trees extracted from the processed image data were compared to the in-situ data collected during the ground surveys.

### **3.5 Step IV: Model Calibration via Canopy-DBH Relationships and Biomass Estimation**

Simple regression analyses were conducted again for the remotely sensed tree data to determine which biophysical parameter of canopy is the best predictor of DBH. The remotely sensed canopy data were correlated with the actual DBH values collected in the field (as stated in section 3.3). The canopy-DBH relationships were used to produce multiple estimates of DBH, and the subsequent estimates were plugged into the species-specific allometric equations to produce AGB estimates.

### **3.6 Step V: Accuracy Assessment**

The remotely sensed tree polygons were overlaid onto the field-based tree polygons, and the attribute tables were spatially joined. The attribute table was exported to Microsoft Excel file format and analyzed in Excel. The OBIA and ITC results were assessed by issuing an IF statement to assign a binary value (0,1) where the species names matched for both the field and remotely sensed features. Values with a 1 indicate that the species classification result was accurate for that feature, whereas a value of 0 indicates that they do not match. The omission error was calculated by subtracting the total number of trees detected from the GIS workflows from the total number of trees collected in the field for each tree species. The commission error was calculated by first sorting the data by species and then assigning a value of 1 if the classifier assigned a species name other than the one stated in the field data. The remotely extracted canopy dimensions were assessed by correlating them to their respective field-based canopy dimensions. Remotely extracted tree heights were compared to the field-based tree heights and ran through a simple linear regression to assess the relationship between the two.

## Chapter Summary

This research was conducted to investigate the potential of canopy structure for the estimation of DBH. Ground data were collected across multiple field surveys and served as the reference values for accuracy assessments of the remotely sensed data. Simple and multiple regression analyses were performed to find the best predictor of DBH for each tree species, and Pearson's correlation analysis was used to quantify the statistical significance of each relationship (by assessing the p-value). The imagery was processed using the SfM method, and the orthomosaics served as the input for a GIS-based workflow to generate polygons representing individual trees with species and canopy information. The remotely sensed canopy parameters were used to predict DBH and the subsequent DBH estimates were used (in conjunction with remotely sensed heights when called for) in species-specific allometric equations to calculate estimates for biomass. All of the estimates were compared to observed values to evaluate the accuracy of this method.

## CHAPTER 4

### RESULTS

This chapter presents a discussion of the results from the field surveys, statistical analyses, GIS workflows, and aboveground biomass (AGB) estimates. The overarching objective of this thesis is to test whether canopy can be effectively used to predict tree trunk diameter and, subsequently, aboveground biomass. Quality ground truth data is necessary for calibrating and evaluating the reliability of the remotely sensed model. This chapter delves into the ground data and then juxtaposes the remotely sensed data with the ground truth data.

#### 4.1 Step I: Field Data Collection

A total of 215 individual tree samples were collected across the ranch, with DBH values ranging from 11cm to 112.5cm, although 90% of the data falls below 66cm. Detailed statistics for the sampled trees are aggregated in Table 1.

Table 3: Summary statistics of the field data

Scientific Name	N	DBH (cm)		Height (m)		Crown Width	
		Mean	SD	Mean	SD	Mean	SD
<i>Quercus douglasii</i>	112	41.13	16.95	9.85	2.86	8.14	3.43
<i>Quercus wislizeni</i>	39	42.22	18.58	7.82	2.88	7.83	2.80
<i>Aesculus californica</i>	64	42.90	16.12	8.51	2.67	7.63	2.62

#### 4.2 Step II: Biomass Calculation and Model Calibration via Regression Analyses

The results of the simple regression analyses indicate that canopy perimeter, crown area, and crown width are moderate to strong predictors of DBH (see Figure 8). All the biophysical parameters of tree canopy are moderate to strong predictors of DBH with R-squared<sup>8</sup> ( $R^2$ ) values

ranging from 0.51 to 0.77. It is important to note that the strongest correlation between tree canopy metric and DBH varied by species. For example, canopy perimeter is the strongest correlate to DBH for blue oaks ( $R^2 = 0.57$ ) and live oaks ( $R^2 = 0.64$ ), yet tree volume—or canopy area multiplied by height ( $CA * H$ )—is the strongest correlate to DBH for buckeye trees ( $R^2 = 0.77$ ). The results of the multiple regression analyses are not shown.<sup>9</sup>

---

<sup>8</sup>  $R^2$  represents the proportion of variance in the dependent variable that is explained by the independent variable(s).

<sup>9</sup> The multiple regression models did not show significantly improved predictive capability over the simple regression models, and the added complexity made it difficult to justify using this approach over a simple regression model.

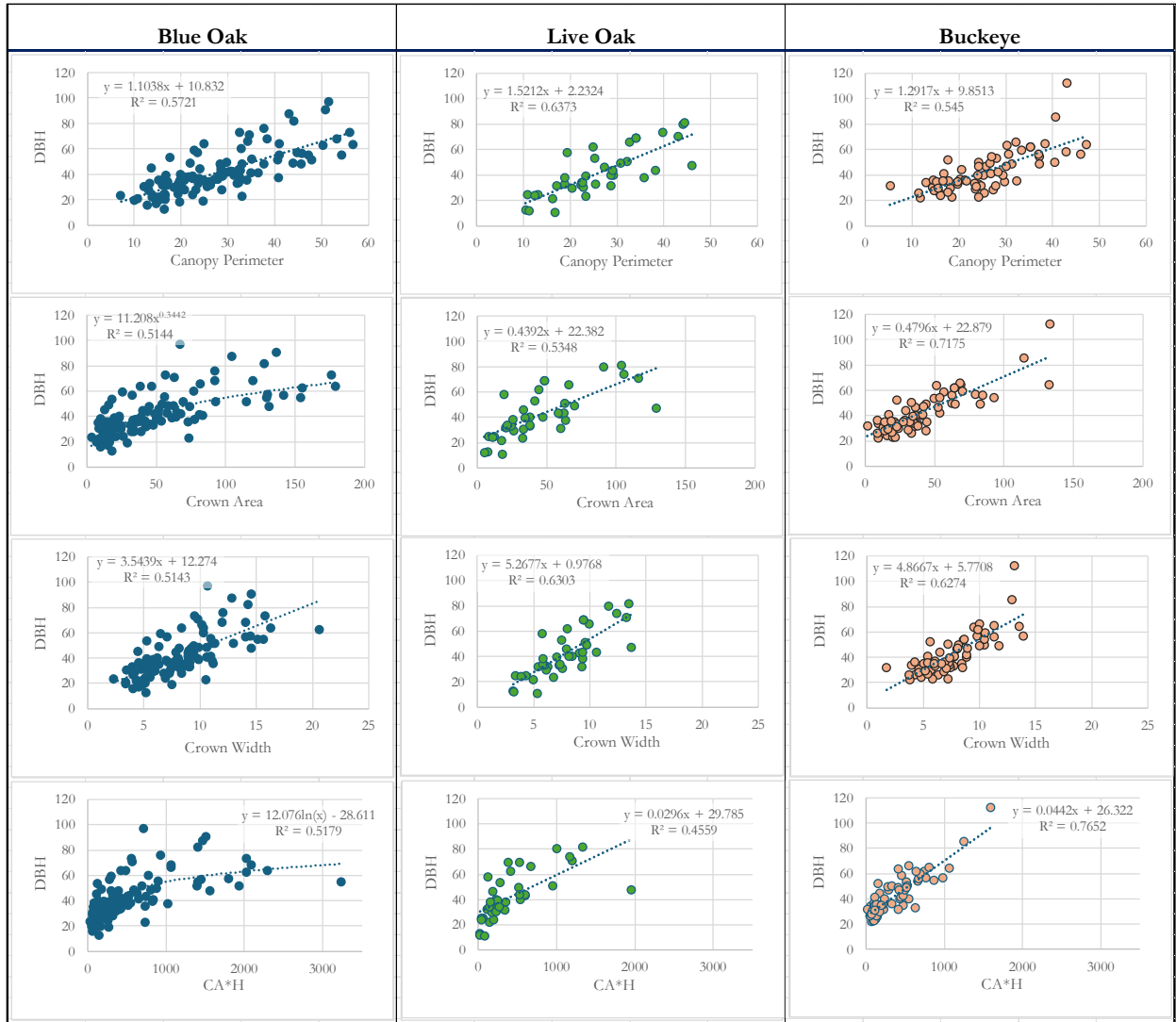


**Figure 8:** Scatterplots for each of the three tree species illustrating the relationship between four different metrics of tree canopy—canopy perimeter, crown area, crown width, and CA \* H—and DBH for the tree polygons generated from the field surveys.



### 4.3 Step III: GIS-Based Workflows

#### OBIA Supervised Classification

The object-based image analysis (OBIA) workflow implemented in this research produced a classified raster dataset, which was subsequently converted to polygons that describe the boundaries of the trees and contain species information as attributes (see Figure 9).

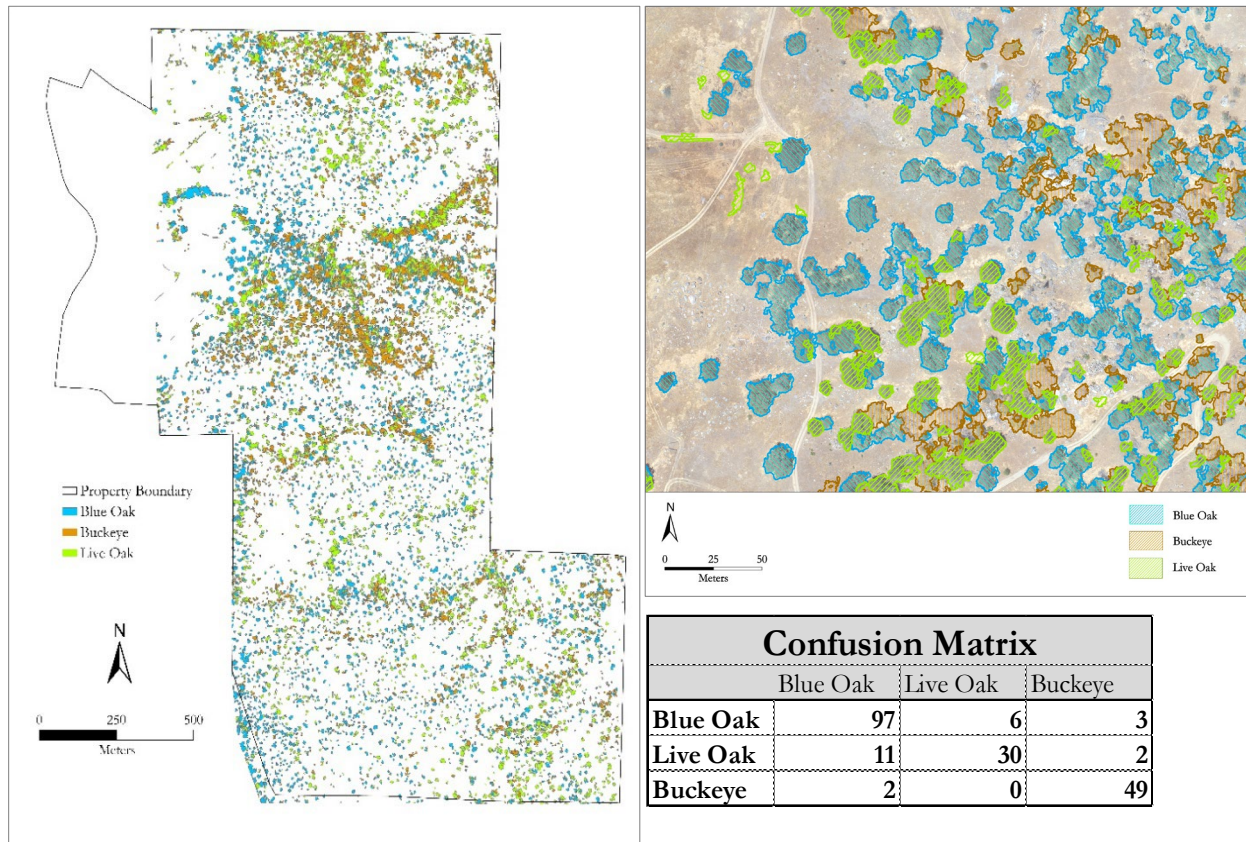


**Figure 9:** Polygons generated from the object-based image analysis workflow for the entire River Ridge Ranch property (at left); polygons generated from the OBIA workflow on a 250 m x 315 m sample region of the ranch (upper right); confusion matrix showcasing the correctly identified trees as well as the commission error (lower right)

## ITC Delineation

The ITC delineation workflow resulted in the identification of 14,986 individual polygons with species information. The canopy perimeter, crown area, and crown width attributes were populated for the tree polygons feature class using the Calculate Geometry function in ArcGIS Pro. Some of the polygons were split in a way such that minuscule areas were included that did not truly describe any trees. To mitigate any inaccuracies caused by this condition, polygons with an area of less than 10 square meters were filtered out. This filtering resulted in 10,811 individual tree polygons being included in the dataset. The tree polygons generated during the in-situ field survey were overlaid with the remotely sensed tree polygons, and the trees that intersected were used for a comparative analysis (see Figure 10).

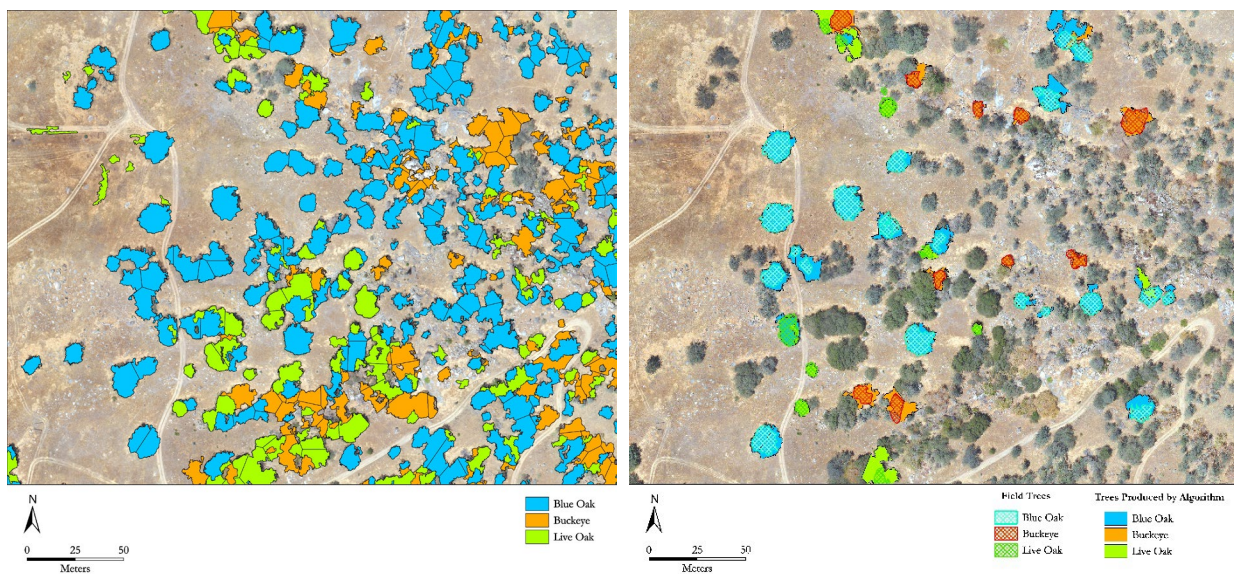


**Figure 10:** Results of the ITC workflow (left) and the field tree polygons overlaying the remotely sensed tree polygons whose canopies overlapped (right).

#### ***4.4 Step IV: Model Calibration via Canopy-DBH Relationships and Biomass Estimation***

The results of these simple regression analyses on the remotely sensed data are shown in Figure 11. Crown area appears to be the overall strongest predictor for all trees; however, the correlation between remotely sensed canopy metrics and DBH was shown to be weak to moderate, with  $R^2$  values ranging from 0.15 to 0.57. Remotely sensed live oak tree canopies had the overall strongest relationships with DBH, with  $R^2$  values ranging from 0.42 to 0.60. Again, as with the field data, the strongest correlate to DBH varied by species, with canopy area performing the best for blue oaks ( $R^2 = 0.29$ ) and buckeye trees ( $R^2 = 0.42$ ), and  $CA * H$  performing the best for live oaks ( $R^2 = 0.60$ ).

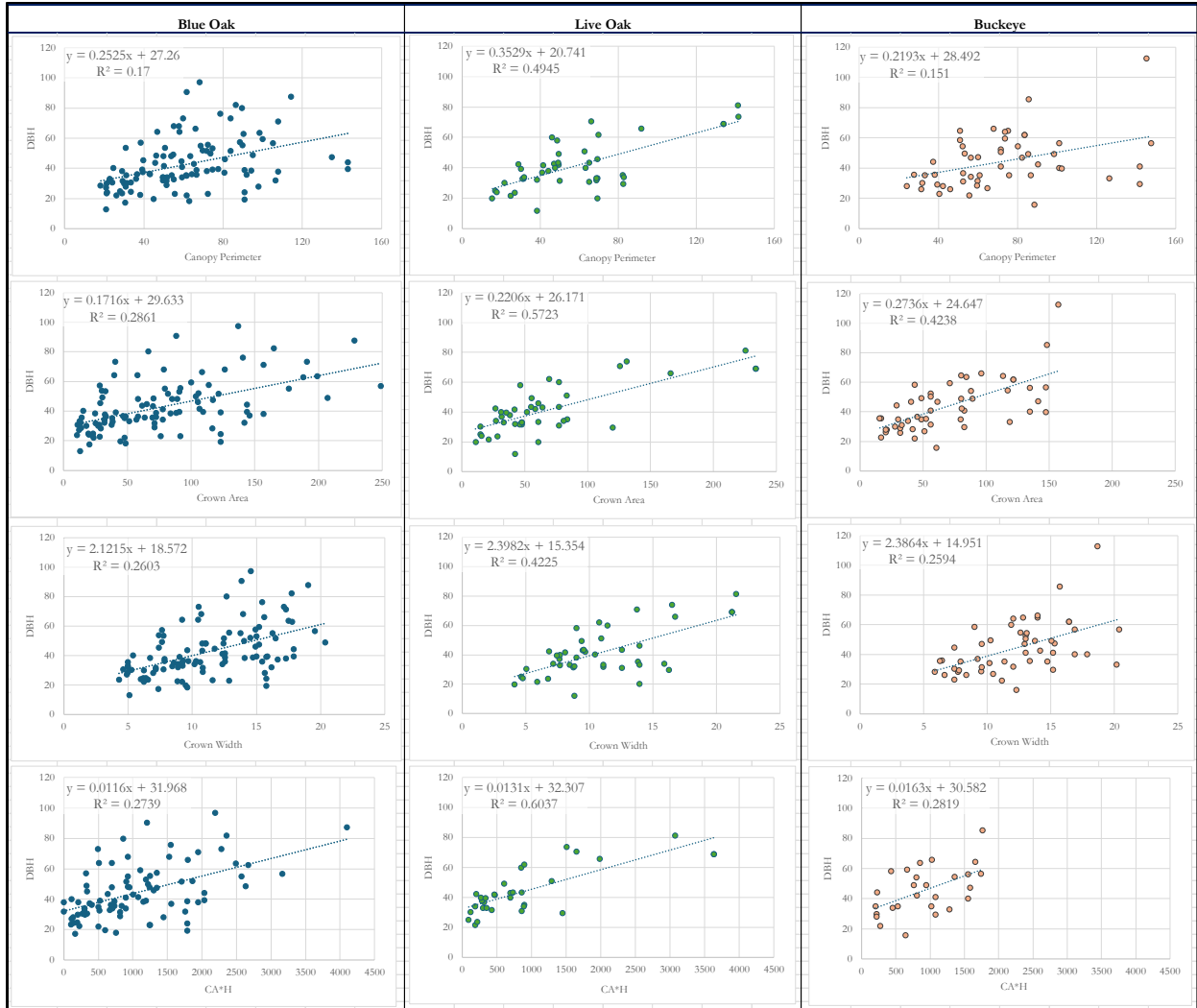


**Figure 11:** Scatterplots for each of the three tree species illustrating the relationship between four different metrics of tree canopy—canopy perimeter, crown area, crown width, and CA \*H—and DBH for the tree polygons generated from the algorithms.

## Aboveground Biomass Results

The observed aboveground biomass was calculated using the species-specific allometric equations and the in-situ field data. These aboveground biomass estimates were calculated using the same species-specific allometric equations but with estimated DBH values resulting from the statistical relationships between canopy and DBH for both the field and remotely sensed data. All aboveground biomass estimates were evaluated against the observed aboveground biomass to ascertain the accuracy of each estimate. The top three estimates are summarized in Table 4. The model using canopy area to predict DBH performed the best in AGB estimation (81.9% accuracy). CA\*H performed the worst (73.4% accuracy)—potentially due to the number of remotely sensed trees that were not assigned a height value—and thus is not shown in Table 4.

**Table 4:** The observed AGB in kilograms for each species as well as the total for all sampled trees (top middle), the aboveground biomass estimates in kilograms using three different methods of estimation for DBH for the field data as well as the overall accuracies of the estimates (bottom left), and the aboveground biomass estimates in kilograms using three different methods of estimation for DBH for the remotely sensed data as well as the overall accuracies of the estimates (bottom right)

### Observed AGB

Species Name	AGB
Blue Oak	129,694.14
Buckeye	77,515.54
Live Oak	37,600.82
<b>Totals</b>	<b>244,810.50</b>

### Field Measured Canopy-Based Estimates

### Remotely Sensed Canopy-Based Estimates

	AGB <sub>1</sub>	AGB <sub>2</sub>	AGB <sub>3</sub>		AGB <sub>1</sub>	AGB <sub>2</sub>	AGB <sub>3</sub>
Blue Oak	104,696.84	115,817.12	117,688.63		107,925.39	106,886.17	102,867.54
Buckeye	72,536.26	70,613.09	69,305.27		58,095.56	55,584.09	52,845.98
Live Oak	33,637.79	34,343.79	34,305.06		34,464.38	30,752.07	31,909.81
<b>Total</b>	<b>210,870.90</b>	<b>220,774.00</b>	<b>221,298.96</b>		<b>200,485.33</b>	<b>193,222.33</b>	<b>187,623.34</b>
<b>Accuracy</b>	<b>86.1%</b>	<b>90.2%</b>	<b>90.4%</b>		<b>81.9%</b>	<b>78.9%</b>	<b>76.6%</b>

Note: AGB<sub>1</sub> – uses the DBH estimate calculated from the relationship between Canopy Area and observed DBH; AGB<sub>2</sub> – uses the DBH estimate calculated from the relationship between Canopy Width and observed DBH; AGB<sub>3</sub> – uses the DBH estimate from the relationship between CA\*H and observed DBH

## 4.5 Step V: Accuracy Assessment of Remotely Sensed Biometrics

### Remotely Extracted Tree Height Results

There were 215 total sampled trees in the field surveys ranging from 3 m to 21 m in height, but only 200 individual trees were detected through the GIS-based workflow, which overlapped the trees sampled in situ. Of the 200 polygons generated from the GIS workflow described in Sections 3.4 and 3.5 of the previous chapter, only 148 were assigned height values using the cell size of 10 m x 10 m. Figure 12 shows the relationship between the remotely sensed tree height estimates and the reference heights from the ground data. The RMSE of the estimate was 3.14 m.

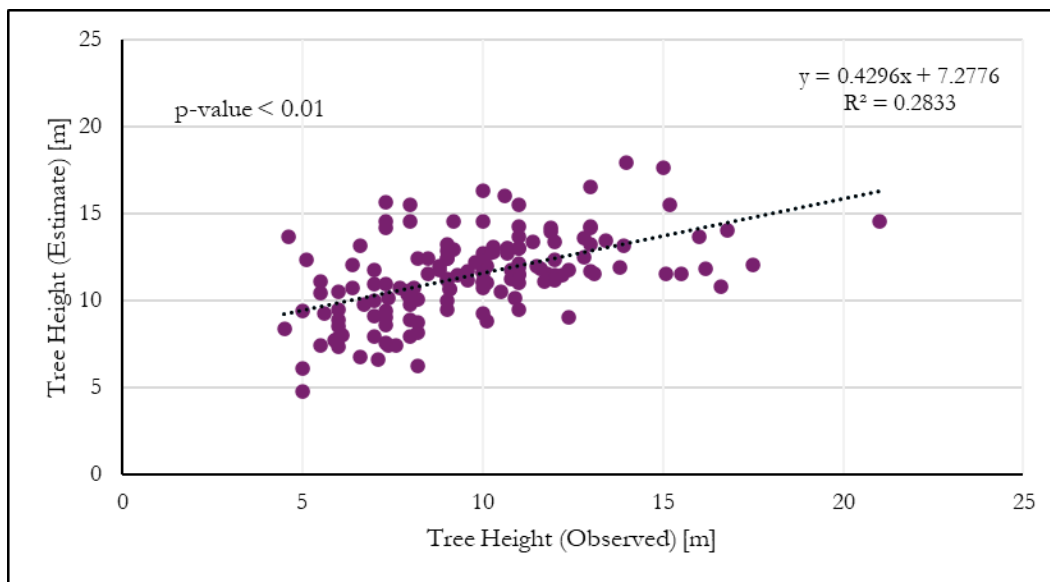


**Figure 12:** The relationship between remotely sensed tree height estimates and the observed tree heights. The  $R^2$  and trendline indicate a weak positive relationship.

### OBIA and ITC Results

An accuracy assessment was carried out in Excel to quantify the reliability of the OBIA and ITC workflows. In total, 81.9% of the trees were correctly identified, with blue oaks—the dominant tree species on the ranch—having the greatest accuracy (86.6%), followed by live oak (76.9%) and buckeye (76.6%). The algorithms employed resulted in a total commission error

(the number of trees detected by the algorithms but were not found to exist based on in-situ observation) of 12%, with live oak having the greatest commission error (30.2%), followed by blue oaks (8.5%), and buckeyes (3.9%). However, buckeye trees had a much larger commission error than is reflected in the comparison with the field data (which will be discussed in further detail in section 5.3). The overall accuracy of the OBIA and ITC workflows for all trees is 84.8%, with blue oaks having the highest overall accuracy (89%), followed by buckeyes (85.2%) and live oaks (73.2%). These data are summarized in Table 5. Moreover, a correlation matrix was generated to test the relationship between the field polygons' attributes and remotely sensed polygons' attributes (see Table 6). All of the biophysical parameters exhibit moderate to strong R values<sup>10</sup>, but only the canopy area has a moderate R<sup>2</sup> value.

**Table 5:** Accuracy Assessment for the detection of individual trees for the three dominant tree species

	Nt	No	Nc	r(%)	p(%)	F1(%)
Blue Oak	97	15	9	86.6%	91.5%	89.0%
Live Oak	30	9	13	76.9%	69.8%	73.2%
Buckeye	49	15	2	76.6%	96.1%	85.2%
All trees	176	39	24	81.9%	88.0%	84.8%

Note: Nt - represents the total number of trees detected that exist in the field; No - the number of trees omitted by the algorithm; Nc - the number of trees that were falsely identified; r - represents the tree detection rate; p - represents the precision of detected trees; and F1 - represents the overall accuracy taking both omission and commission in consideration.

**Table 6:** Correlation matrix illustrating the relationships between the field-based and remotely extracted biometrics.

	Height	Perimeter	Area	Width	CA*H
R	0.533	0.477	0.667	0.614	0.631
R-sq	0.284	0.227	0.445	0.377	0.398

<sup>10</sup> "R" represents the correlation coefficient, which measures the strength and direction of the linear relationship between two variables. It ranges from -1 to 1.

## CHAPTER 5

### DISCUSSION

The primary goal of this thesis was to develop and evaluate a method for using remotely sensed variables in field-derived, species-specific allometric equations to quantify aboveground biomass. This thesis consisted of a number of steps: (1) the collection of in-situ ground truthing data; (2) biomass calculation and model calibration with regression analyses in order to predict DBH from tree canopy dimensions; (3) photogrammetry and GIS-based workflows to produce remotely sensed parameters including tree species, height, and biophysical metrics of canopy at the individual tree level; (4) model calibration via regression analyses using the remotely sensed canopy variables and in-situ measurements of DBH, followed by biomass estimation; (5) accuracy assessment of the remotely sensed data (generated in step 3) and biomass estimates (generated in step 4).

The theory examined here is that canopy-based DBH estimates can accurately assess AGB, thus demonstrating greater efficiency and cost-effectiveness than conventional field methods. The AGB estimates that this author derived from the canopy-DBH relationships performed reasonably well, with the best model (using crown area) only underestimating AGB by 18.1%. This result far exceeded this author's initial expectations, particularly in light of the fact that AGB and carbon content are often overestimated in California (Badgley et al., 2021), and that other biomass estimation models are commonly used beyond their initial scope leading to errors reportedly as high as 240% (Weiskittel et al., 2017). As it stands, the model explored in this thesis can quantify key forest parameters with a reasonable degree of accuracy. However, the improper delineation of individual tree crowns (ITCs) where canopies overlap certainly decreased the overall reliability of the model. Recognizing this limitation, one way to increase



the reliability of this model is to implement an accurate method for delineating tree crowns. The object-based image analysis, in and of itself, generated an output that can be converted to polygons representing individual trees with accurate species information and canopy data where tree canopies did not overlap. This is a promising finding as over half of the world's wooded areas have a canopy cover of less than 50% (Mlambo et al. 2017).

This study found that tree canopy is a moderate to strong predictor of DBH. This insight suggests potential pathways for enhancing the efficiency and accuracy of forest inventories. This study further found that canopy area is the best metric to use for the estimation of DBH compared to canopy perimeter, crown width, and  $CA * H$ . Canopy area provides a more comprehensive understanding of the overall canopy structure as canopy shapes do not always conform to a predictable circular or convex shape but can take on elliptical or more complex forms. Canopy area also remained relatively consistent in both the in-situ and RS data, while canopy perimeter, crown width, and  $CA * H$  vary moderately between the two datasets. Leveraging canopy area information and employing automated techniques to delineate trees at the individual level offers potential for gathering inventory data through sUAS remote sensing. The techniques employed in this thesis can be used to successfully collect forest parameters in wooded lands where tree canopies do not overlap.

### **5.1 Comparison With Existing Studies**

Three previous studies have explored the use of drone-based tree measurements for the extraction of key forest parameters (e.g. tree species, individual tree crowns and canopy dimensions, canopy-based estimates of DBH, and AGB). In general, the results achieved in this thesis are comparable to the other studies with some differences attributed to environmental factors such as canopy complexity. In the study by Iizuka et al. (2017), tree canopy was found to

be a strong predictor of DBH. Their study area consisted of a Japanese cypress forest, a coniferous forest with a closed canopy structure. Despite the constraints of ground exposure caused by the closed canopy, the RMSE of their remotely extracted tree heights was a reasonable 1.71 m, but the correlation between their observed tree heights and extracted tree heights was poor ( $R^2 = 0.208$ ). DBH showed a strong correlation with both canopy width ( $R^2 = 0.7786$ ) and canopy area ( $R^2 = 0.7923$ ) across a range of DBH values from 11 to 58 cm. The findings of this thesis compare well with Iizuka's, especially when considering the higher complexity of the broadleaved canopies studied. The tree heights generated from the field data have a slightly better correlation ( $R^2 = 0.28$ ) with the field heights compared to Iizuka; however, the RMSE is much higher at 3.14 m, thus indicating that the SfM method has poor predictive performance for tree heights.

The open canopy structure of River Ridge Ranch should have improved the digital elevation products and resultant CHM when juxtaposed to Iizuka's closed canopy structure cypress forest, yet the RMSE is almost twice as large. This error could be due to the manner in which tree heights were extracted (explained in section 3.4). The method to extract tree heights may need to be adjusted to yield better tree height estimates. This thesis found that tree canopy is highly correlated with DBH for the field data, but only moderately so for the remotely sensed data. It also found canopy area to be the strongest relative to DBH for the remotely sensed data, as well as the most consistent parameter between the in-situ and remotely sensed data. This strongly suggests that canopy area may be the best biophysical parameter of the tree canopy to use for DBH estimation. On the other hand, the individual tree crown (ITC) delineation method used in this thesis was found to be oversimplified, and the results were thus suboptimal. This likely significantly impacted the DBH-canopy relationship for the remotely sensed data, which

could explain the lower predictive power of most of the remotely sensed canopy parameters compared to Iizuka et al. (2017). For this reason, further exploration of this method should focus on improving ITC delineation results.

Xu et al. (2020) successfully classified the dominant tree species in a subtropical forest containing a mix of coniferous and broadleaved trees in southwest China using multispectral aerial imagery and structural information<sup>11</sup>. When looking at the individual tree level, their classifier had an overall accuracy of 66.3%. The SVM classifier used in this thesis had an overall accuracy of 84.8%. The higher accuracy presented in this thesis may be due to the lower complexity of the landscape. While the referenced authors' study site was characterized by a closed canopy structure and eight dominant tree species including both coniferous and broadleaved trees, the study area used for this thesis only has three dominant tree species and an overall open canopy structure. This finding indicates that high-resolution multispectral imagery can be used to accurately classify tree species for an open canopy forest/woodland but may have a limited applicability to a more complex, closed-canopy landscape.

The research of Jones et al. (2020) attempted to estimate mangrove biomass using sUAS-derived tree biometrics. While their study does not offer any results for comparison with this thesis, their research suggested a promising new approach for biomass estimation assuming that the relationship between tree canopy, height, and DBH can be better defined. This thesis successfully defined statistically significant canopy-DBH relationships between the three dominant tree species on River Ridge Ranch, and found that estimates of aboveground biomass (AGB) that are based on the demonstrated canopy-DBH correlation can reach accuracies slightly better than 80%.

---

<sup>11</sup> Structural information refers to metrics such as tree height and canopy dimensions that can be extracted at the individual tree level.

## 5.2 Limitations

### Ground Truth Data

Some limitations were identified that are associated with the ground truth data used in this thesis. The reliability of the tree height data collected in the field has not yet been assessed. Moreover, the in-situ dataset used in this thesis was initially intended to serve as a broad-based inventory of not only live trees, but also grasses, shrubs, and dead trees at River Ridge Ranch—over 600 features in all. To reduce the effect of this limitation, features other than live trees have largely been filtered out leaving a total of 215 remaining features in the in-situ dataset. Some of the dead trees were difficult to filter out, posing a problem as it could lead to false omission errors. The field surveys also took place across several years and varying seasons, introducing errors. For example, the tree polygons from the field survey sometimes varied from the tree canopies identified in the sUAS imagery because growth had occurred in the interval of time that had passed between the field survey and the sUAS imaging missions. If the tree canopies do not match up, there is an elevated potential for error as the relationship between canopy (as derived from the sUAS imagery) and DBH is the primary relationship explored in this thesis. Efforts were taken to minimize this error by manually editing the polygons that comprise the field data so that they align better with the canopies visible in the aerial imagery. An improved sampling scheme could have eliminated some of the biases introduced in this thesis.

### Digital Elevation Products

A crucial aspect when estimating tree height from 3D models built with the SfM method is to generate a DTM of dependable quality. The heights of surface objects are calculated by subtracting the pure terrain data from a DSM, so if the DTM is inaccurate, the heights of surface objects will be inaccurate. Several studies have shown that Structure from Motion is comparable to LiDAR in flatter terrain with a sparse distribution of surface targets with appreciable height

(Wallace et al. 2016; Goodbody et al. 2017; Mlambo et al. 2017; Iglhaut et al. 2019). However, when the terrain and land cover becomes more complex, especially if tree canopies begin to overlap, the reliability of SfM deteriorates. Dense tree canopy cover can obstruct the view of the ground surface. The occlusion of the ground surface makes it very difficult to identify ground points, and in such cases interpolating and accurately reconstructing the terrain is particularly challenging. This limitation can lead to gaps or over-interpolation of the DTM by the SfM software, rendering SfM feasible only in areas with an open canopy structure (i.e., less than 50% cover). This condition is observed in the DTM and resulting CHM generated for this thesis. The areas that exhibited the lowest accuracy were tributary stream channels with dense overlapping tree canopies. However, areas of the ranch with open canopies tended to display more accurate height and canopy values. Considering that more than half of the world's wooded lands have less than 50% canopy cover (Mlambo et al. 2017), the above finding suggests that there are many regions where SfM can be used successfully.

### Object-Based Image Analysis

OBIA offers several advantages over pixel-based analysis, including better handling of spatial and contextual information, reduced sensitivity to noise, and improved accuracy in feature extraction and classification (OpenAI 2024). Additionally, and more notably, it yields an output that can be readily converted to polygons from which individual tree crowns can be extracted—at least where individual tree canopies do not overlap. The OBIA workflow adopted for this thesis proved to be an excellent tool based on its ease of use and accuracy, and ArcGIS Pro's imagery classification wizard guides users through the entire process. The species classification results of the OBIA workflow were 84.8% accurate. Nonetheless, some critical factors that should be considered when classifying tree species using OBIA were uncovered. Firstly, tree

phenology plays a vital role in the algorithm's ability to classify tree species. For example, blue oaks are winter-deciduous, interior live oaks are evergreen, and buckeyes are summer-deciduous. The images used for analysis within this thesis were acquired in June (early summer) when the buckeye trees' leaves tend to start browning and dropping. Consequently, the buckeyes' canopies are not full, and the leaves are spectrally similar to the surrounding bare ground. The gaps in buckeye trees' canopies and the browning leaves confused the classification algorithm and resulted in neighboring areas of bare ground being incorporated into the buckeye class. A few large areas of ground were incorrectly identified as buckeye and had to be manually filtered out—although this could be done automatically by using the CHM to filter out regions less than 3 meters in height. Another important consideration with object-based image analysis is that reliable training data is vital for creating an accurate model. With object-based image analysis, it is preferable that the training samples are not spectrally pure; instead, they should denote the entirety of an object including pixels that have spectral signatures that vary from that of the object of interest in the scene. Also, it is essential to use approximately the same number of samples per training class; oversaturating one class can affect the model's accuracy. One final thing to ensure is that a thorough and representative set of bare ground samples is obtained as this is an essential factor in evaluating the accuracy of the classification results.

The OBIA workflow in ArcGIS Pro showed a great deal of promise in classifying the dominant tree species with five-band multispectral imagery on River Ridge Ranch. The classification results could be improved by incorporating more reliable CHM data derived from, for example, a LiDAR point cloud, using more training samples per class, and using an image where buckeye trees are not shedding their leaves. The OBIA and segmentation method alone

demonstrate considerable potential for generating individual tree polygons with species attributes and canopy data in areas with an open tree canopy cover.

### ITC Delineation

Individual tree canopy (ITC) delineation is necessary to partition a forest's canopy into individual tree crowns, thereby enabling quantitative analysis and mapping of tree-level attributes and spatial patterns within forested areas. Previous research has explored several methods, but most appear tailored for coniferous trees with uncomplicated, convex canopy shapes. Watershed segmentation is presently the most popular individual tree segmentation algorithm, but it often results in over-segmentation and can be complicated to carry out (Qin et al., 2022). The method used in this thesis was adapted from a technique that uses negative curvature values from a LiDAR-derived CHM to delineate individual tree boundaries (Argomosa et al. 2016). Their model was developed using a stand of trees in a coniferous plantation. One major limitation of using plantations is their uniform size, which is typically not representative of natural forest ecosystems. Additionally, coniferous trees have a conical shape, resulting in only one true tree top and making it easier to detect negative curvature values. In contrast, oaks have more complex shapes making it challenging to identify a single true tree top and utilize negative curvature values effectively. Oak tree canopy shape is vastly different and far more complicated than the convex shape of coniferous tree canopies. Therefore, the methodology was modified in that the Thiessen polygons were simply used to split tree canopies where multiple tree canopies overlapped. While this modified approach is overly simplistic, it is easy to perform and results in more accurate polygons than the ones generated from the species classification alone in areas where canopies overlap. It is important to emphasize that this modified approach is far from optimal and has resulted in polygons with highly inaccurate shapes where the canopy cover is

dense. Areas with an open canopy structure exhibited far more accurate polygons, which resulted solely from the OBIA workflow.

The study area mainly consists of open canopy woodland, and most of the trees surveyed in the field and used for the accuracy assessment were trees whose canopies did not overlap. This resulted in an accuracy assessment that reflects the algorithm's ability to effectively map tree species and canopy metrics for open canopy woodlands; however, based on visual inspection, the algorithm performs poorly in regions with a closed canopy structure.

### **5.3 sUAS and SfM for Forestry Applications**

SfM holds a great deal of promise for forestry and research applications, and the use of sUAS for image acquisition missions offers the added advantage of high flexibility. The capability for high temporal resolution can be used to carry out increased-frequency remote sensing surveys to account for phenological changes. Operating an sUAS for forestry tasks includes several vital steps: mission planning, setting up components, flying the UAV, and downloading data. Thanks to modern sUAS being equipped with mission planning software, image acquisition missions can be largely autonomous, minimizing the need for constant user intervention and reducing the potential for human error. The rapid learning curve of contemporary sUAS flight planning and management applications makes them highly useful for forest monitoring. The commercial sUAS market has significantly reduced the knowledge gap between experienced users and novices by advancing fully autonomous sUAS operation. Moreover, the processing of sUAS imagery using the SfM algorithm can be readily automated with little required user input. Batch scripts allow users to pre-define calculation parameters and execute them sequentially. SfM photogrammetry therefore presents an easily accessible and highly versatile approach to obtaining detailed 3D terrain and land cover data. Through SfM,



ordinary forestry professionals gain the ability to perform real-time data analysis with minimal investments in both hardware and software. Typically, the expenses associated with buying, operating, and upkeeping an sUAS are comparatively much lower than those incurred with piloted aerial imaging missions, or regularly procuring high-resolution satellite imagery. Using the SfM method with sUAS-acquired imagery demonstrates great potential as a low-cost and accurate remote sensing method for forest parameter acquisition and biomass calculation.

#### **5.4 Conclusions**

The current state of biomass estimation faces many challenges in terms of labor, efficiency, cost, technical expertise, accuracy, and precision. The ability to effectively measure forest parameters, however, is a high priority for many land managers. As such, much research has investigated the use of remote sensing to quantify forest structure to decrease costs, alleviate labor, and increase efficiency (Iizuka et al. 2017; Jones et al. 2020; Xu et al. 2020). This thesis developed a procedure to use remotely sensed canopy biometrics to indirectly quantify AGB in an oak woodland via DBH estimates. The procedures outlined herein were used to remotely extract various metrics of tree canopy and successfully quantify aboveground biomass within a reasonable margin of error. Using SfM, researchers can generate outputs that can be used to accurately extract canopy and height data for wooded lands, particularly those with an open canopy structure.

This thesis sought to evaluate the efficacy of high-resolution aerial imagery and SfM photogrammetry to quantify forest parameters—specifically aboveground biomass. This was achieved via statistical analysis, remote sensing and digital image processing, and GIS-based techniques to classify tree species and extract biophysical parameters at the individual tree level. The statistical analyses performed by this author indicate that canopy size has a strong

correlation to DBH, and derivative estimates of DBH can be used in species-specific allometric equations to approximate aboveground biomass. The polygons produced from the GIS-based workflows match up well with the field-derived polygons. The species classification workflow exhibited a high degree of accuracy (compared with the field data) apart from the image classification errors associated with the unusual buckeye tree phenology. One of the benefits of sUAS and SfM is the flexibility to plan image acquisition missions at a frequency to address phenological changes. It is suggested that any follow-up research should address tree phenology by using a winter or spring image for the object-based image classification. Ideally, more emphasis should be placed on ITC delineation, as it is crucial for accurately extracting canopy metrics; however, it is an aspect that is highly technical and requires a great deal of research, time, and effort. A field sampling scheme must be clearly defined to address sampling biases and account for potential confounding variables. Notwithstanding these limitations, this thesis demonstrates the potential for using high-resolution sUAS imagery to extract biophysical parameters of tree canopy for use in estimating aboveground biomass, particularly in open canopy woodlands.

## **APPENDICES**

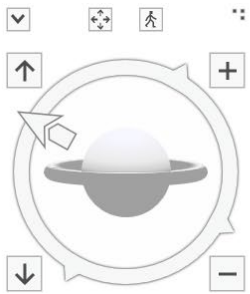
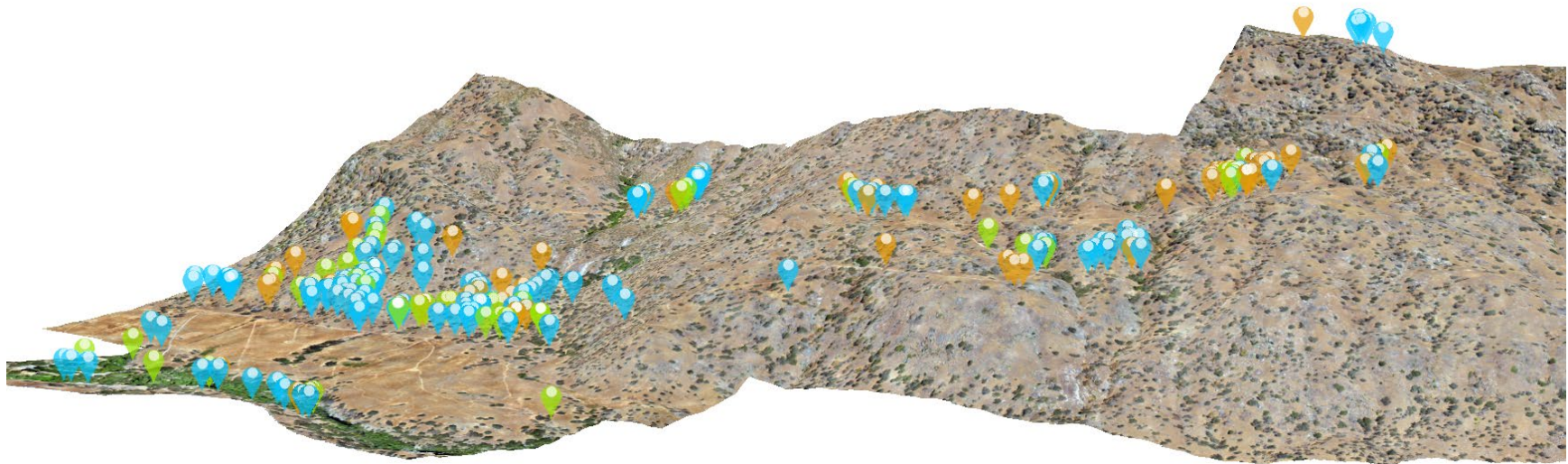
## **APPENDIX A**



Figure 1: This image was taken during a ground survey in the higher elevations of the ranch. It shows the steep topography and general landscape of the ranch, as well as the pasture located in the valley.



Figure 2: This image was acquired during another ground survey near the bottom of the hillside. It shows off the topography and distribution of trees on the ranch.








-  Blue Oak
-  Buckeye
-  Live Oak


Figure 3: 3D representation of the landscape of River Ridge Ranch. Shows the distribution of trees sampled for the field data and gives an idea of the ranch's terrain. Bottom left shows the orientation of the 3D model.


## **APPENDIX B**



 **Important:** Click on the different icons for:

 Help to analyze the results in the Quality Report

 Additional information about the sections

 Click [here](#) for additional tips to analyze the Quality Report











## Summary



Project	2022-06-15_all
Processed	2022-06-28 09:31:07
Camera Model Name(s)	S.O.D.A._10.6_5472x3648 (RGB)
Average Ground Sampling Distance (GSD)	4.12 cm / 1.62 in

## Quality Check



 <b>Images</b>	median of 50000 keypoints per image	
 <b>Dataset</b>	3570 out of 3570 images calibrated (100%), all images enabled, 2 blocks	
 <b>Camera Optimization</b>	0.94% relative difference between initial and optimized internal camera parameters	
 <b>Matching</b>	median of 10450.6 matches per calibrated image	
 <b>Georeferencing</b>	yes, no 3D GCP	

Number of Calibrated Images	out of 3570
Number of Geolocated Images	out of 3570



## Calibration Details



### ② Initial Image Positions

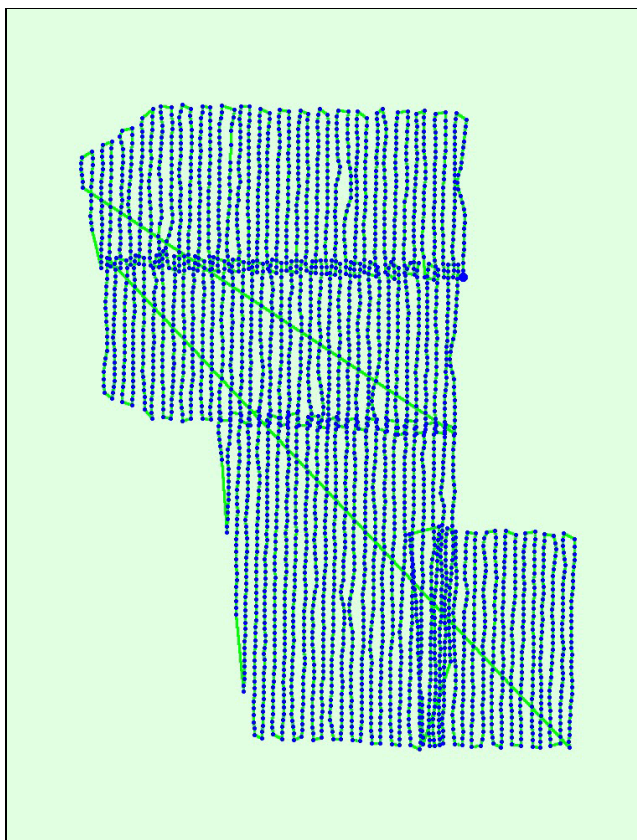
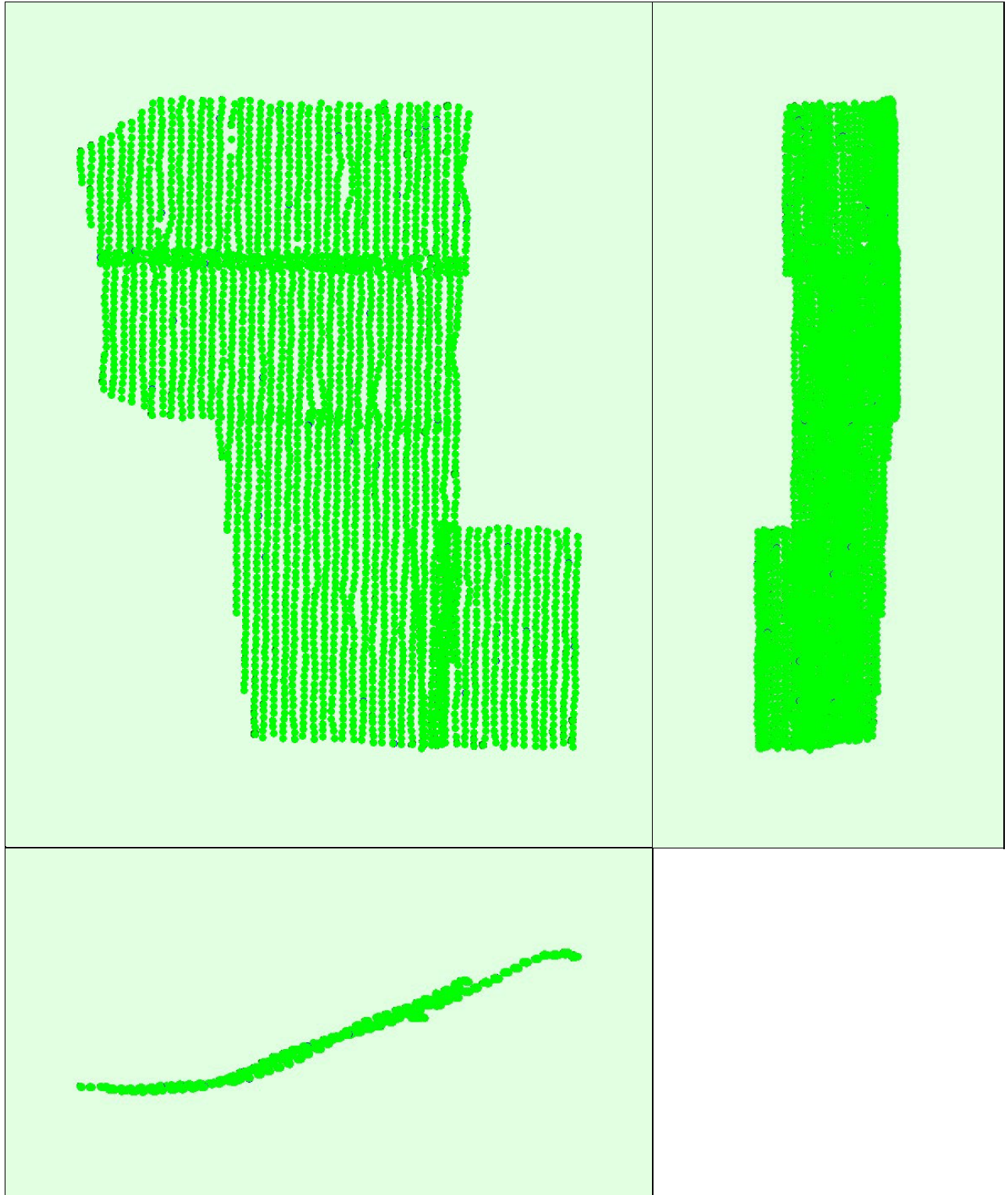


Figure 2: Top view of the initial image position. The green line follows the position of the images in time starting from the large blue dot.

### ② Computed Image/GCPs/Manual Tie Points Positions





Uncertainty ellipses 1000x magnified

Figure 3: Offset between initial (blue dots) and computed (green dots) image positions as well as the offset between the GCPs initial positions (blue crosses) and their computed positions (green crosses) in the top-view (XY plane), front-view (XZ plane), and side-view (YZ plane). Dark green ellipses indicate the absolute position uncertainty of the bundle block adjustment result.

## Absolute camera position and orientation uncertainties

	X [m]	Y [m]	Z [m]	Omega [degree]	Phi [degree]	Kappa [degree]
Mean	0.007	0.009	0.007	0.004	0.003	0.003
Sigma	0.002	0.001	0.001	0.001	0.001	0.001

## Bundle Block Adjustment Details

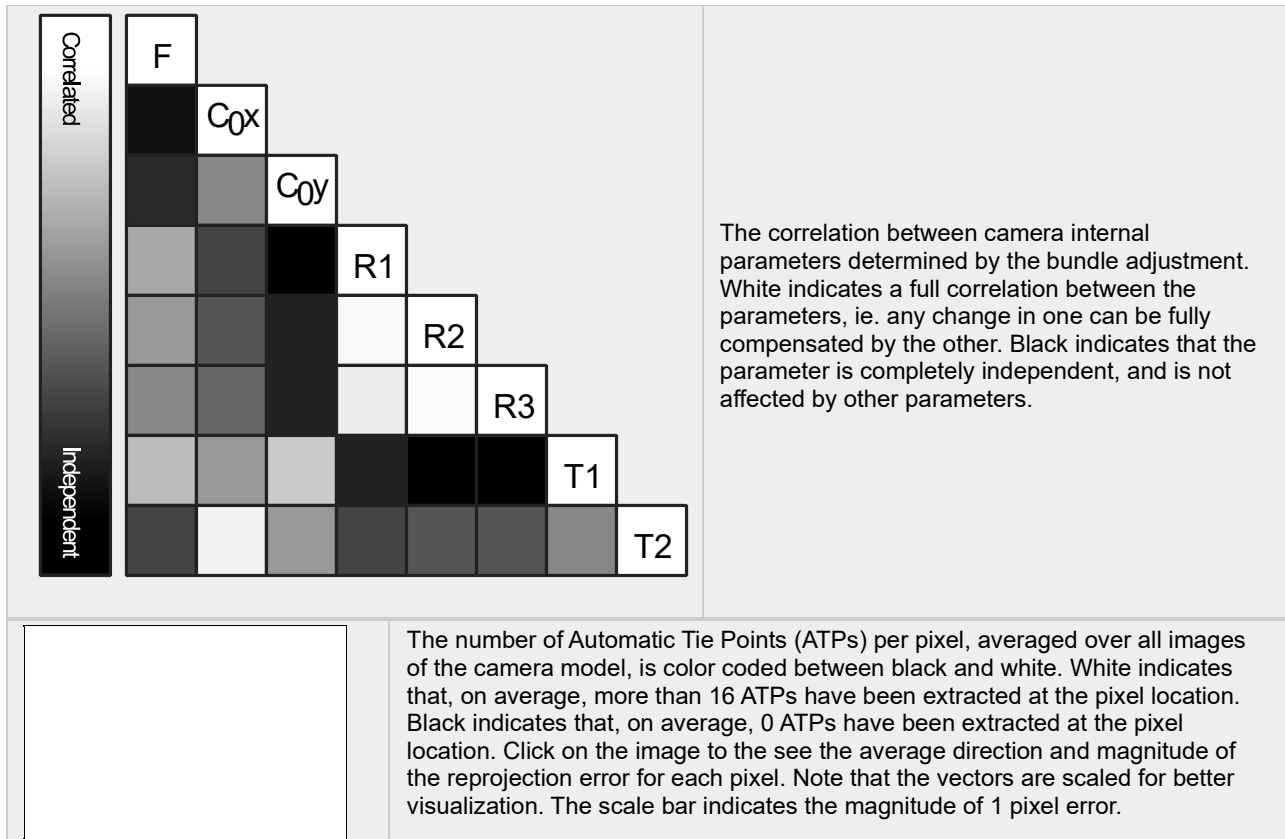


Number of 2D Keypoint Observations for Bundle Block Adjustment	38761002
Number of 3D Points for Bundle Block Adjustment	15278462
Mean Reprojection Error [pixels]	0.151

## Internal Camera Parameters S.O.D.A.\_10.6\_5472x3648 (RGB). Sensor Dimensions: 13.133 [mm] x 8.755 [mm]

EXIF ID: S.O.D.A.\_10.6\_5472x3648

	Focal Length	Principal Point x	Principal Point y	R1	R2	R3	T1	T2
Initial Values	4430.420 [pixel] 10.633 [mm]	2725.000 [pixel] 6.540 [mm]	1811.670 [pixel] 4.348 [mm]	0.033	-0.209	0.315	0.000	0.000
Optimized Values	4388.388 [pixel] 10.532 [mm]	2761.017 [pixel] 6.626 [mm]	1820.488 [pixel] 4.369 [mm]	0.038	-0.238	0.342	0.001	0.000
Uncertainties (Sigma)	0.017 [pixel] 0.000 [mm]	0.027 [pixel] 0.000 [mm]	0.018 [pixel] 0.000 [mm]	0.000	0.000	0.000	0.000	0.000



## ? 2D Keypoints Table

	Number of 2D Keypoints per Image	Number of Matched 2D Keypoints per Image
Median	50000	10451
Min	50000	67
Max	50000	26099
Mean	50000	10857

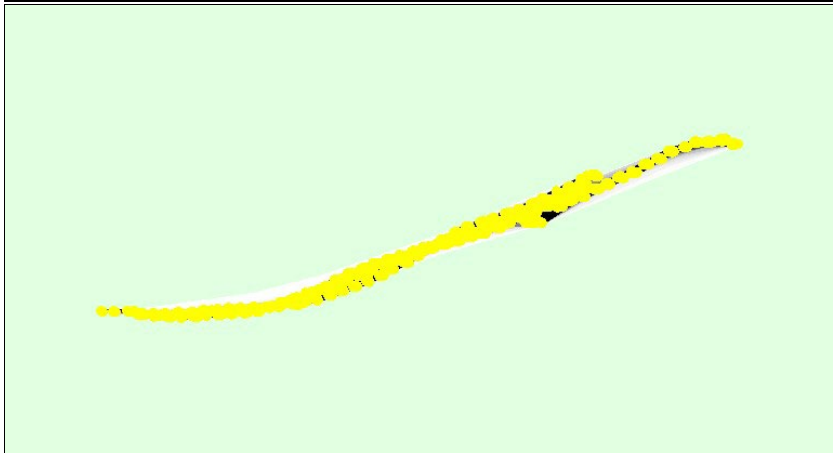
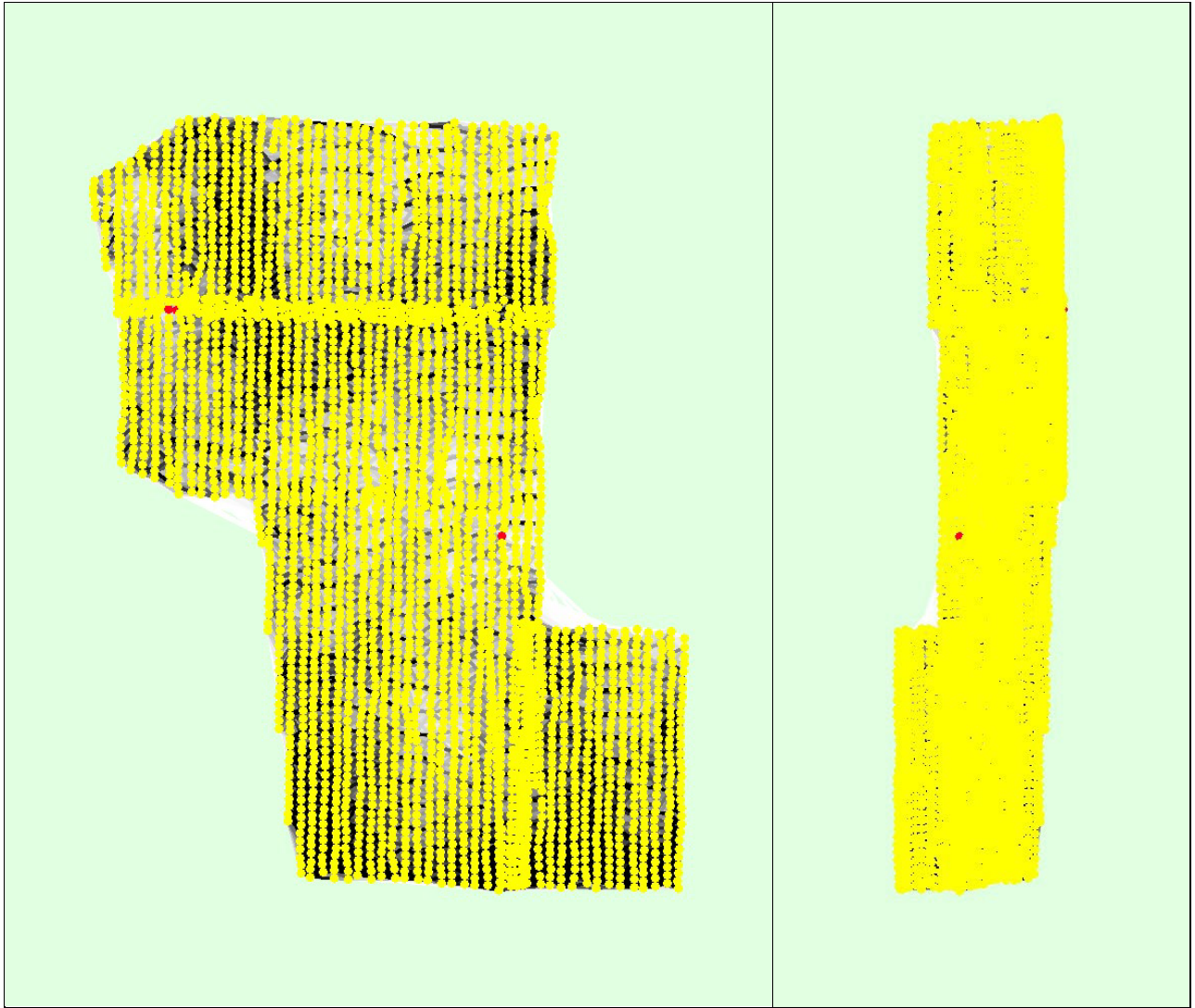
## ? 3D Points from 2D Keypoint Matches

	Number of 3D Points Observed
In 2 Images	11452545
In 3 Images	2181845
In 4 Images	762446
In 5 Images	345542
In 6 Images	185438
In 7 Images	110448
In 8 Images	69535

In 9 Images	46317
In 10 Images	31926
In 11 Images	22778
In 12 Images	16261
In 13 Images	12093
In 14 Images	9012
In 15 Images	6761
In 16 Images	5228
In 17 Images	4008
In 18 Images	3107
In 19 Images	2500
In 20 Images	1945
In 21 Images	1582
In 22 Images	1299
In 23 Images	962
In 24 Images	823
In 25 Images	638
In 26 Images	510
In 27 Images	427
In 28 Images	357
In 29 Images	310
In 30 Images	281
In 31 Images	214
In 32 Images	188
In 33 Images	146
In 34 Images	135
In 35 Images	100
In 36 Images	101
In 37 Images	78
In 38 Images	73
In 39 Images	56
In 40 Images	54
In 41 Images	42
In 42 Images	41
In 43 Images	23
In 44 Images	33
In 45 Images	29
In 46 Images	25
In 47 Images	30

In 48 Images	18
In 49 Images	21
In 50 Images	10
In 51 Images	15
In 52 Images	15
In 53 Images	15
In 54 Images	12
In 55 Images	5
In 56 Images	9
In 57 Images	9
In 58 Images	4
In 59 Images	1
In 60 Images	4
In 61 Images	2
In 62 Images	5
In 63 Images	5
In 64 Images	1
In 65 Images	3
In 66 Images	2
In 67 Images	4
In 68 Images	1
In 70 Images	1
In 71 Images	1
In 72 Images	2
In 73 Images	1
In 76 Images	2
In 77 Images	1
In 88 Images	1

## 2D Keypoint Matches



Number of matches

25 222 444 666 888 1111 1333 1555 1777 2000

Figure 5: Computed image positions with links between matched images. The darkness of the links indicates the number of matched 2D keypoints between the images. Bright links indicate weak links and require manual tie points or more images.

## Geolocation Details

### 2 Absolute Geolocation Variance

Min Error [m]	Max Error [m]	Geolocation Error X [%]	Geolocation Error Y [%]	Geolocation Error Z [%]
-	-1.07	0.00	0.00	0.00
-1.07	-0.86	0.00	0.00	0.00
-0.86	-0.64	0.00	0.00	0.00
-0.64	-0.43	0.00	0.00	0.00
-0.43	-0.21	0.00	0.00	0.00
-0.21	0.00	51.29	50.70	49.80
0.00	0.21	48.71	49.30	50.20
0.21	0.43	0.00	0.00	0.00
0.43	0.64	0.00	0.00	0.00
0.64	0.86	0.00	0.00	0.00
0.86	1.07	0.00	0.00	0.00
1.07	-	0.00	0.00	0.00
<b>Mean [m]</b>		0.000003	-0.000049	0.000169
<b>Sigma [m]</b>		0.016025	0.018006	0.017285
<b>RMS Error [m]</b>		0.016025	0.018006	0.017286

Min Error and Max Error represent geolocation error intervals between -1.5 and 1.5 times the maximum accuracy of all the images. Columns X, Y, Z show the percentage of images with geolocation errors within the predefined error intervals. The geolocation error is the difference between the initial and computed image positions. Note that the image geolocation errors do not correspond to the accuracy of the observed 3D points.

### 2 Relative Geolocation Variance

Relative Geolocation Error	Images X [%]	Images Y [%]	Images Z [%]
[-1.00, 1.00]	96.44	95.74	96.13
[-2.00, 2.00]	99.72	99.05	99.94
[-3.00, 3.00]	99.92	99.72	99.94
<b>Mean of Geolocation Accuracy [m]</b>	0.034068	0.034068	0.035161
<b>Sigma of Geolocation Accuracy [m]</b>	0.007672	0.007672	0.011773

Images X, Y, Z represent the percentage of images with a relative geolocation error in X, Y, Z.

Geolocation Orientational Variance	RMS [degree]
------------------------------------	--------------



Omega	1.327
Phi	1.046
Kappa	2.022

Geolocation RMS error of the orientation angles given by the difference between the initial and computed image orientation angles.

## Initial Processing Details


### System Information

Hardware	CPU: AMD Ryzen Threadripper 3970X 32-Core Processor RAM: 256GB GPU: NVIDIA GeForce RTX 3070 (Driver: 30.0.14.7212)
Operating System	Windows 10 Education, 64-bit

### Coordinate Systems

Image Coordinate System	WGS 84
Output Coordinate System	WGS 84 / UTM zone 11N

### Processing Options

Detected Template	 SODA 3D Oak Savanna*
Keypoints Image Scale	Full, Image Scale: 1
Advanced: Matching Image Pairs	Aerial Grid or Corridor
Advanced: Matching Strategy	Use Geometrically Verified Matching: yes
Advanced: Keypoint Extraction	Targeted Number of Keypoints: Custom, Number of Keypoints: 50000
Advanced: Calibration	Calibration Method: Geolocation Based Internal Parameters Optimization: All External Parameters Optimization: All Rematch: Custom, yes

## Point Cloud Density details

### Processing Options

Image Scale	multiscale, 1 (Original image size, Slow)
Point Density	Optimal
Minimum Number of Matches	2
3D Textured Mesh Generation	no
LOD	Generated: no
Advanced: Image Groups	group1
Advanced: Use Processing Area	no
Advanced: Use Annotations	no

Time for Point Cloud Densification	17h:02m:18s
Time for Point Cloud Classification	NA
Time for 3D Textured Mesh Generation	NA

## Results

Number of Processed Clusters	3
Number of Generated Tiles	156
Number of 3D Densified Points	2096788613
Average Density (per m <sup>3</sup> )	48.79

## DSM, Orthomosaic and Index Details

### Processing Options

DSM and Orthomosaic Resolution	10 [cm/pixel]
DSM Filters	Noise Filtering: yes Surface Smoothing: yes, Type: Medium
Raster DSM	Generated: yes Method: Triangulation Merge Tiles: yes
Orthomosaic	Generated: yes Merge Tiles: yes GeoTIFF Without Transparency: yes Google Maps Tiles and KML: no
Raster DTM	Generated: yes Merge Tiles: yes
DTM Resolution	10 [cm/pixel]
Time for DSM Generation	17m:50s
Time for Orthomosaic Generation	01h:29m:48s
Time for DTM Generation	04h:25m:14s
Time for Contour Lines Generation	00s
Time for Reflectance Map Generation	00s
Time for Index Map Generation	00s

## **APPENDIX C**

# Quality Report



Generated with PIX4Dmapper version 4.7.5

**Important:** Click on the different icons for:

- Help to analyze the results in the Quality Report
- Additional information about the sections

Click [here](#) for additional tips to analyze the Quality Report

## Summary



Project	Merged
Processed	2022-07-18 09:57:12
Camera Model Name(s)	RedEdge-M_5.5_1280x960 (Blue), RedEdge-M_5.5_1280x960 (Green), RedEdge-M_5.5_1280x960 (Red), RedEdge-M_5.5_1280x960 (NIR), RedEdge-M_5.5_1280x960 (Red edge)
Rig name(s)	«RedEdge-M»
Average Ground Sampling Distance (GSD)	11.21 cm / 4.42 in
Time for Initial Processing (without report)	01h:26m:58s

## Quality Check



<b>Images</b>	median of 10000 keypoints per image	
<b>Dataset</b>	25773 out of 25825 images calibrated (99%), 40 images disabled, 2 blocks	
<b>Camera Optimization</b>	0.07% relative difference between initial and optimized internal camera parameters	
<b>Matching</b>	median of 2265.99 matches per calibrated image	
<b>Georeferencing</b>	yes, no 3D GCP	

Number of Calibrated Images	out of 25865
Number of Geolocated Images	out of 25865

## Calibration Details



### Initial Image Positions



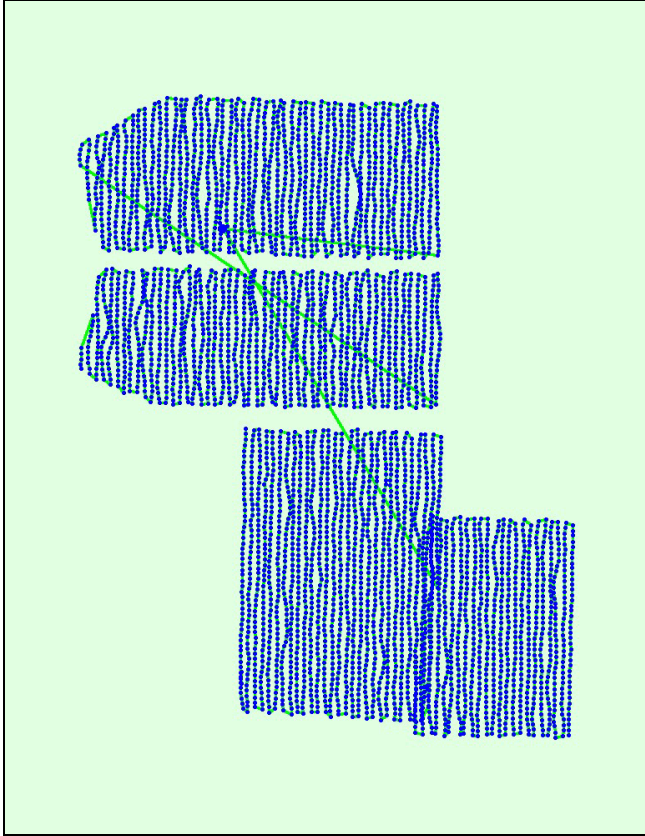
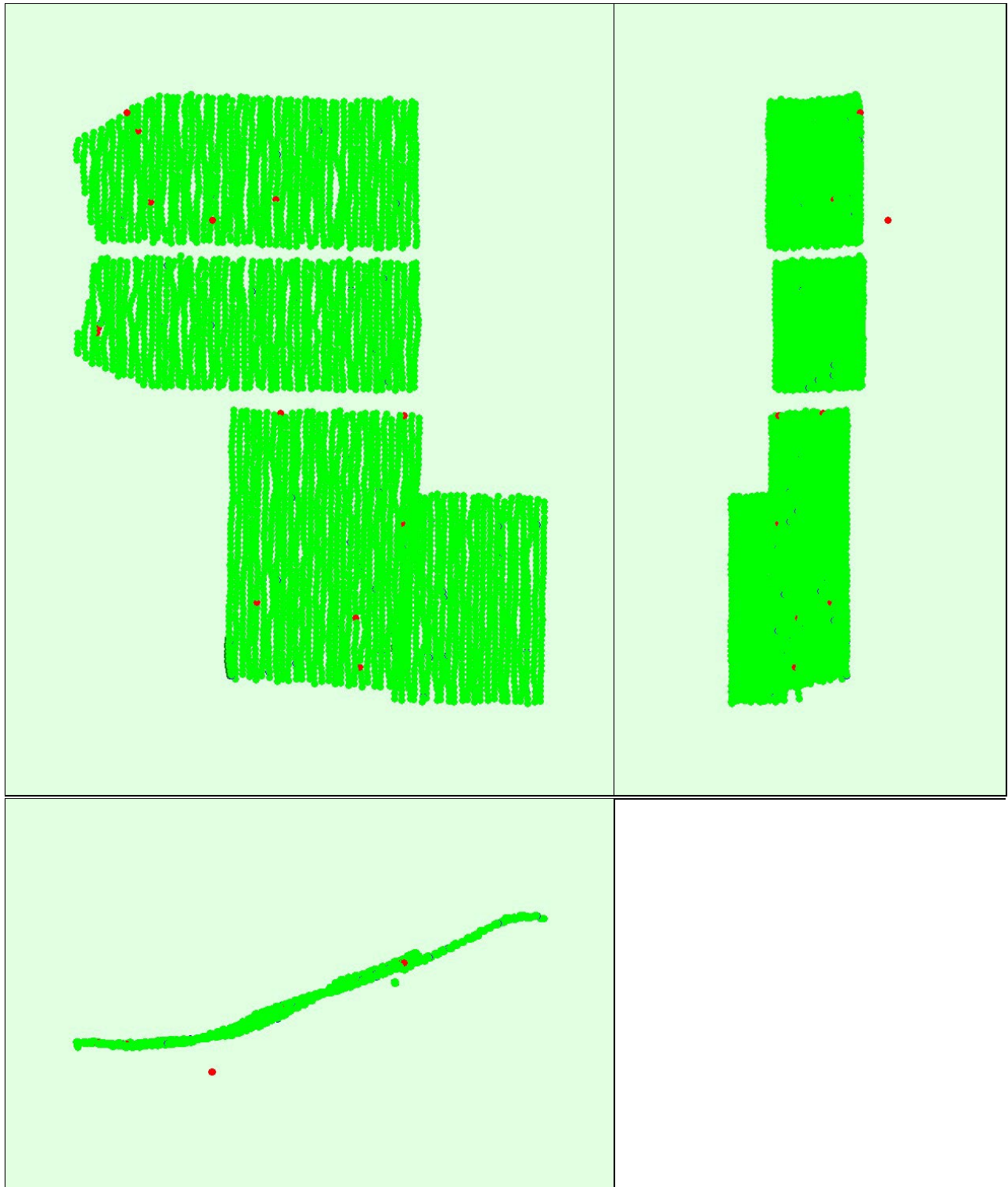


Figure 2: Top view of the initial image position. The green line follows the position of the images in time starting from the large blue dot.



Uncertainty ellipses 500x magnified

Figure 3: Offset between initial (blue dots) and computed (green dots) image positions as well as the offset between the GCPs initial positions (blue crosses) and their computed positions (green crosses) in the top-view (XY plane), front-view (XZ plane), and side-view (YZ

plane). Red dots indicate disabled or uncalibrated images. Dark green ellipses indicate the absolute position uncertainty of the bundle block adjustment result.

### 🔍 Absolute camera position and orientation uncertainties ℹ️

	X [m]	Y [m]	Z [m]	Omega [degree]	Phi [degree]	Kappa [degree]
Mean	0.010	0.010	0.007	0.004	0.004	0.003
Sigma	0.001	0.001	0.001	0.002	0.002	0.003

## Bundle Block Adjustment Details ℹ️



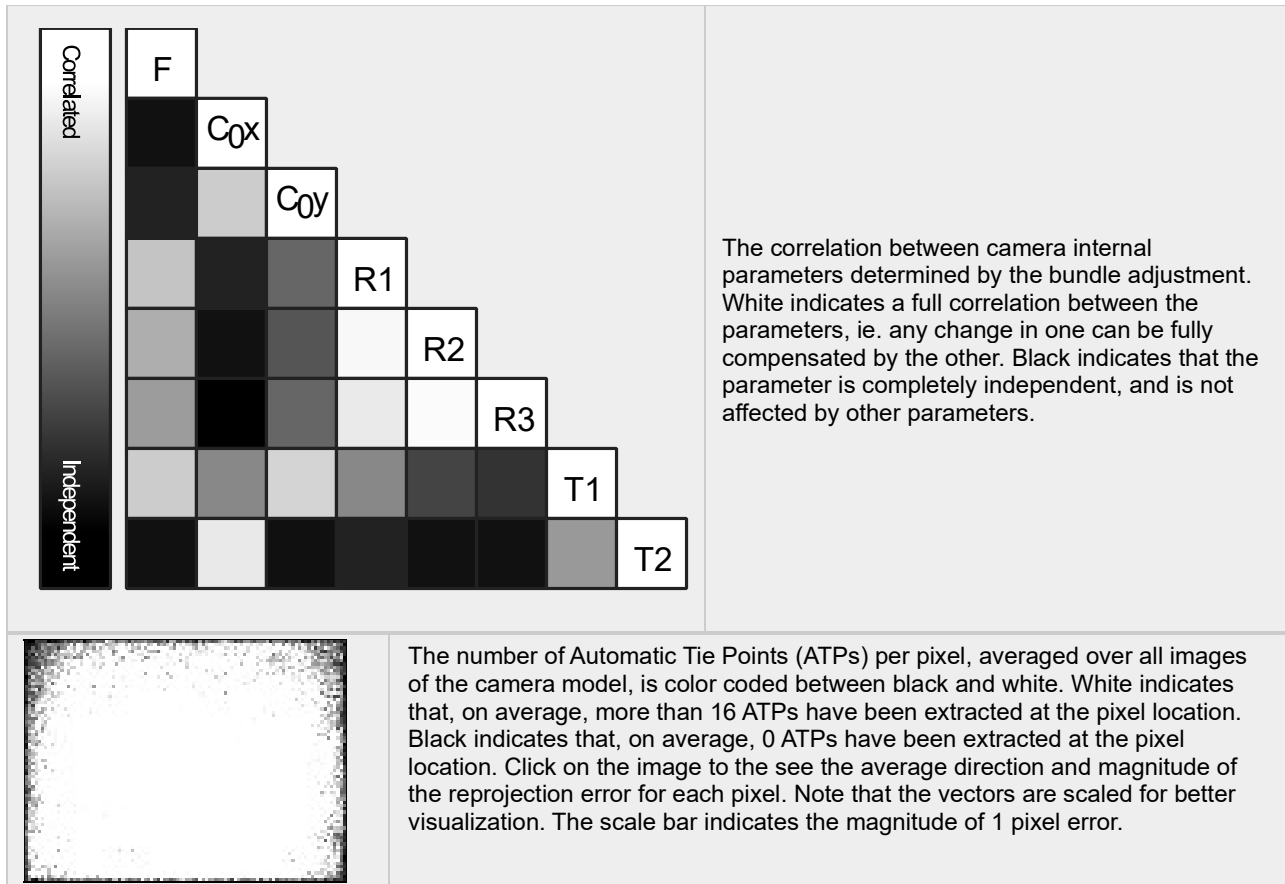
Number of 2D Keypoint Observations for Bundle Block Adjustment	16420551
Number of 3D Points for Bundle Block Adjustment	5763384
Mean Reprojection Error [pixels]	0.092

### Internal Camera Parameters

#### RedEdge-M\_5.5\_1280x960 (Blue). Sensor Dimensions: 4.800 [mm] x 3.600 [mm] ℹ️

EXIF ID: RedEdge-M\_5.5\_1280x960

	Focal Length	Principal Point x	Principal Point y	R1	R2	R3	T1	T2
Initial Values	1445.135 [pixel] 5.419 [mm]	639.853 [pixel] 2.399 [mm]	490.589 [pixel] 1.840 [mm]	- 0.101	0.158	- 0.056	0.001	- 0.001
Optimized Values	1444.074 [pixel] 5.415 [mm]	640.922 [pixel] 2.403 [mm]	488.425 [pixel] 1.832 [mm]	- 0.097	0.133	0.001	0.001	- 0.000
Uncertainties (Sigma)	0.044 [pixel] 0.000 [mm]	0.106 [pixel] 0.000 [mm]	0.086 [pixel] 0.000 [mm]	0.001	0.005	0.010	0.000	0.000



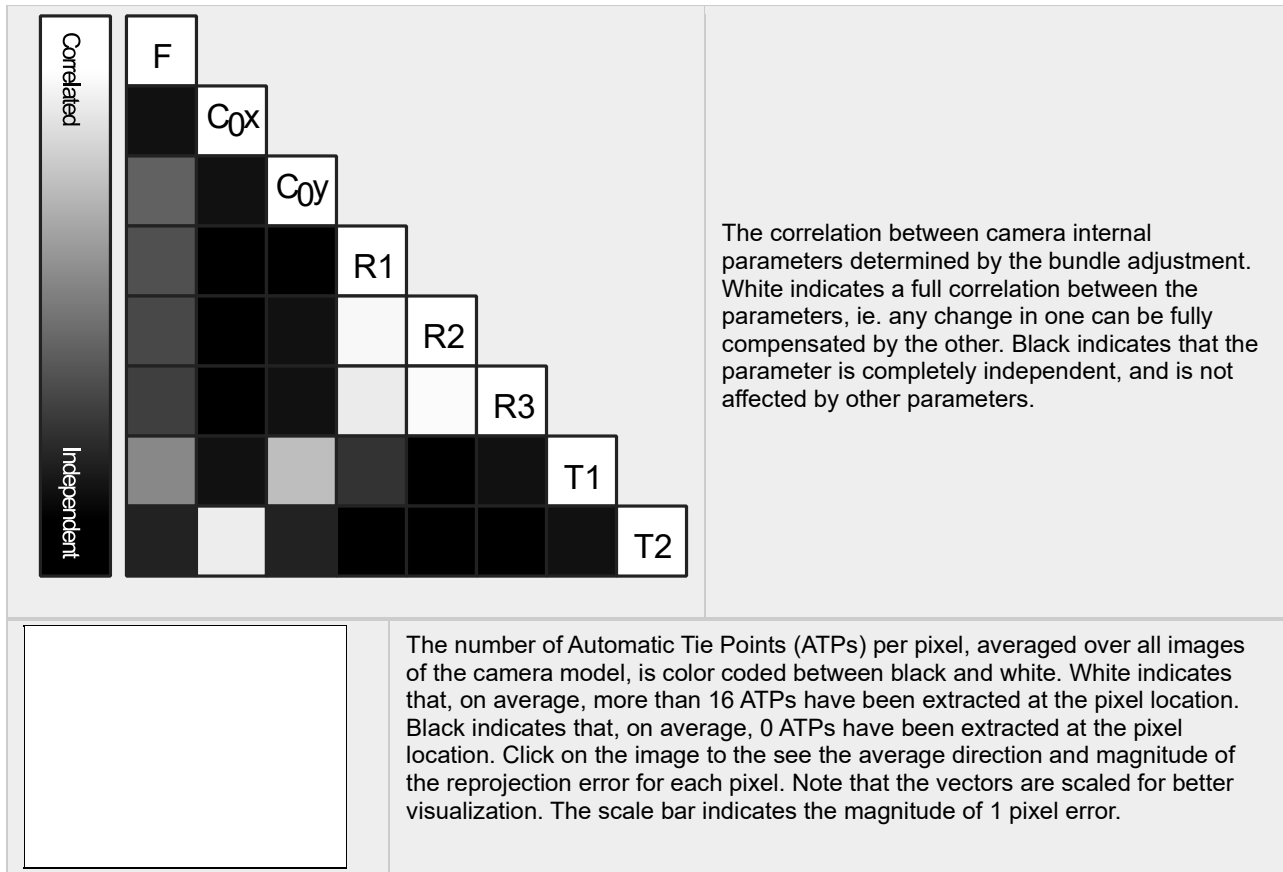
## Internal Camera Parameters

RedEdge-M\_5.5\_1280x960 (Green). Sensor Dimensions: 4.800 [mm] x 3.600 [mm]

EXIF ID: RedEdge-M\_5.5\_1280x960

	Focal Length	Principal Point x	Principal Point y	R1	R2	R3	T1	T2
Initial Values	1447.164 [pixel] 5.427 [mm]	635.720 [pixel] 2.384 [mm]	493.176 [pixel] 1.849 [mm]	-0.100	0.155	-0.055	0.000	-0.000
Optimized Values	1446.025 [pixel] 5.423 [mm]	636.198 [pixel] 2.386 [mm]	492.117 [pixel] 1.845 [mm]	-0.098	0.143	-0.030	-0.000	0.000
Uncertainties (Sigma)	0.017 [pixel] 0.000 [mm]	0.016 [pixel] 0.000 [mm]	0.013 [pixel] 0.000 [mm]	0.000	0.001	0.002	0.000	0.000



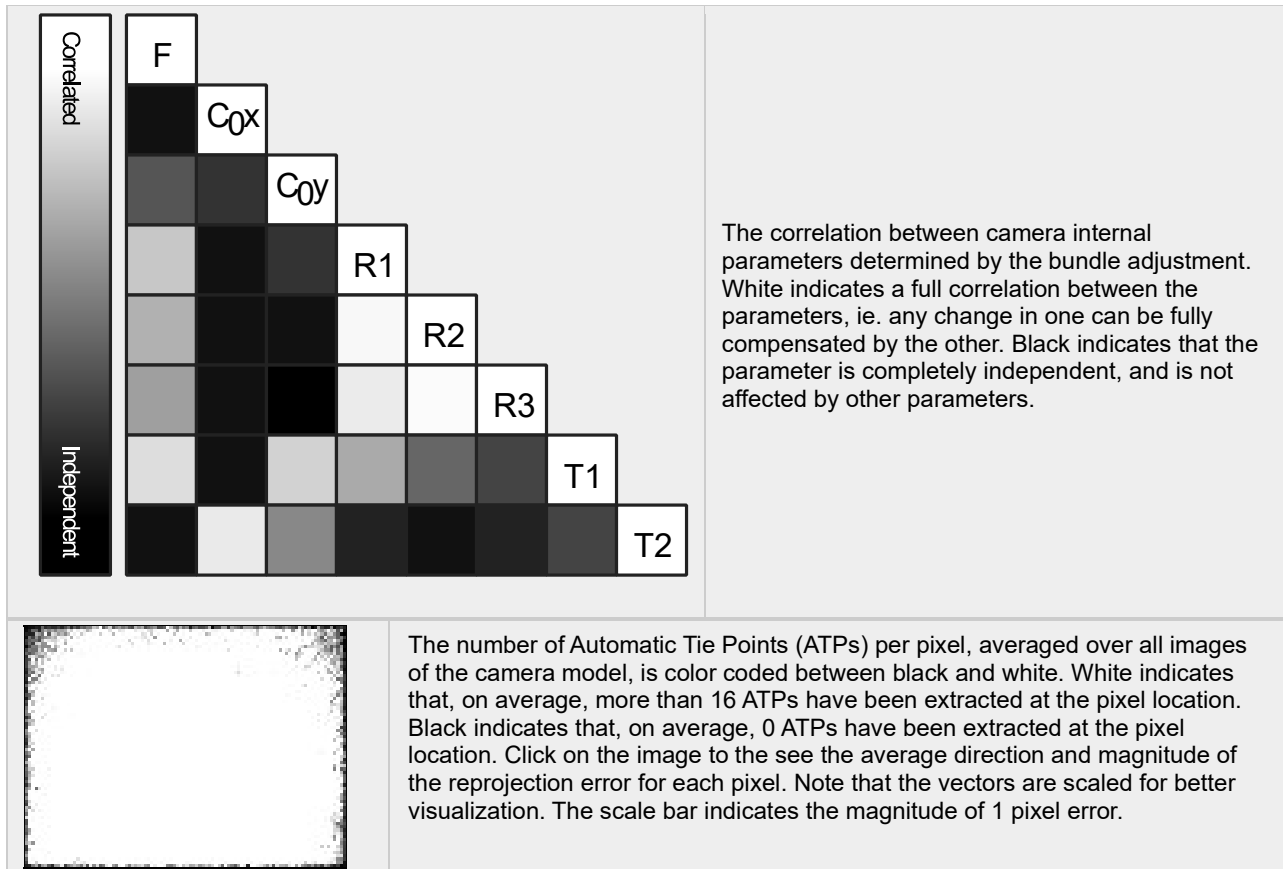


## Internal Camera Parameters

RedEdge-M\_5.5\_1280x960 (Red). Sensor Dimensions: 4.800 [mm] x 3.600 [mm]

EXIF ID: RedEdge-M\_5.5\_1280x960

	Focal Length	Principal Point x	Principal Point y	R1	R2	R3	T1	T2
Initial Values	1446.009 [pixel] 5.423 [mm]	634.437 [pixel] 2.379 [mm]	480.096 [pixel] 1.800 [mm]	-0.106	0.154	-0.044	-0.000	-0.001
Optimized Values	1444.918 [pixel] 5.418 [mm]	634.869 [pixel] 2.381 [mm]	478.472 [pixel] 1.794 [mm]	-0.103	0.142	-0.023	-0.000	-0.000
Uncertainties (Sigma)	0.046 [pixel] 0.000 [mm]	0.112 [pixel] 0.000 [mm]	0.089 [pixel] 0.000 [mm]	0.001	0.005	0.010	0.000	0.000



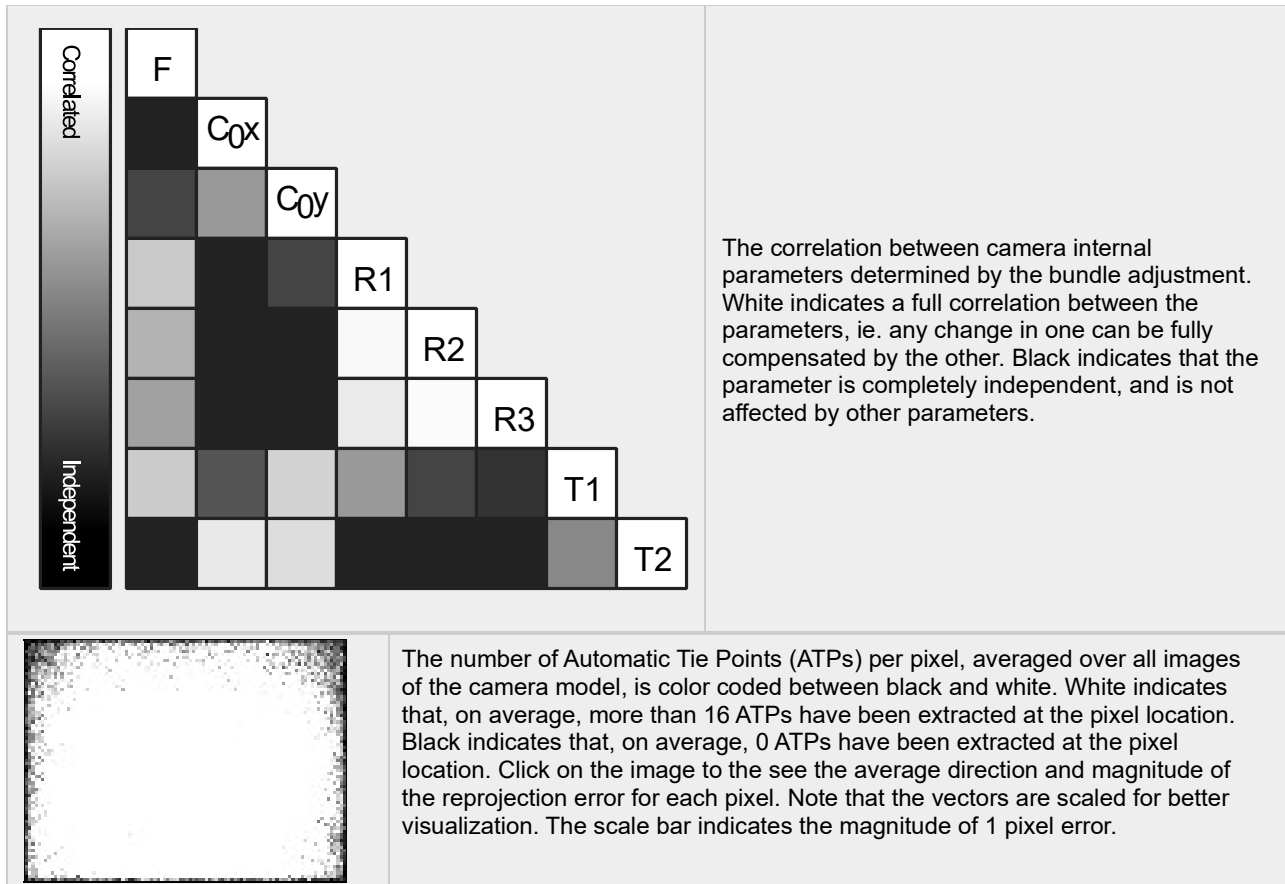
**Internal Camera Parameters**

**RedEdge-M\_5.5\_1280x960 (NIR). Sensor Dimensions: 4.800 [mm] x 3.600 [mm]**



EXIF ID: RedEdge-M\_5.5\_1280x960

	Focal Length	Principal Point x	Principal Point y	R1	R2	R3	T1	T2
Initial Values	1454.389 [pixel] 5.454 [mm]	636.600 [pixel] 2.387 [mm]	486.000 [pixel] 1.823 [mm]	-0.107	0.158	-0.058	-0.000	-0.000
Optimized Values	1453.483 [pixel] 5.451 [mm]	637.277 [pixel] 2.390 [mm]	484.344 [pixel] 1.816 [mm]	-0.103	0.134	-0.000	-0.001	-0.000
Uncertainties (Sigma)	0.050 [pixel] 0.000 [mm]	0.124 [pixel] 0.000 [mm]	0.099 [pixel] 0.000 [mm]	0.001	0.005	0.012	0.000	0.000

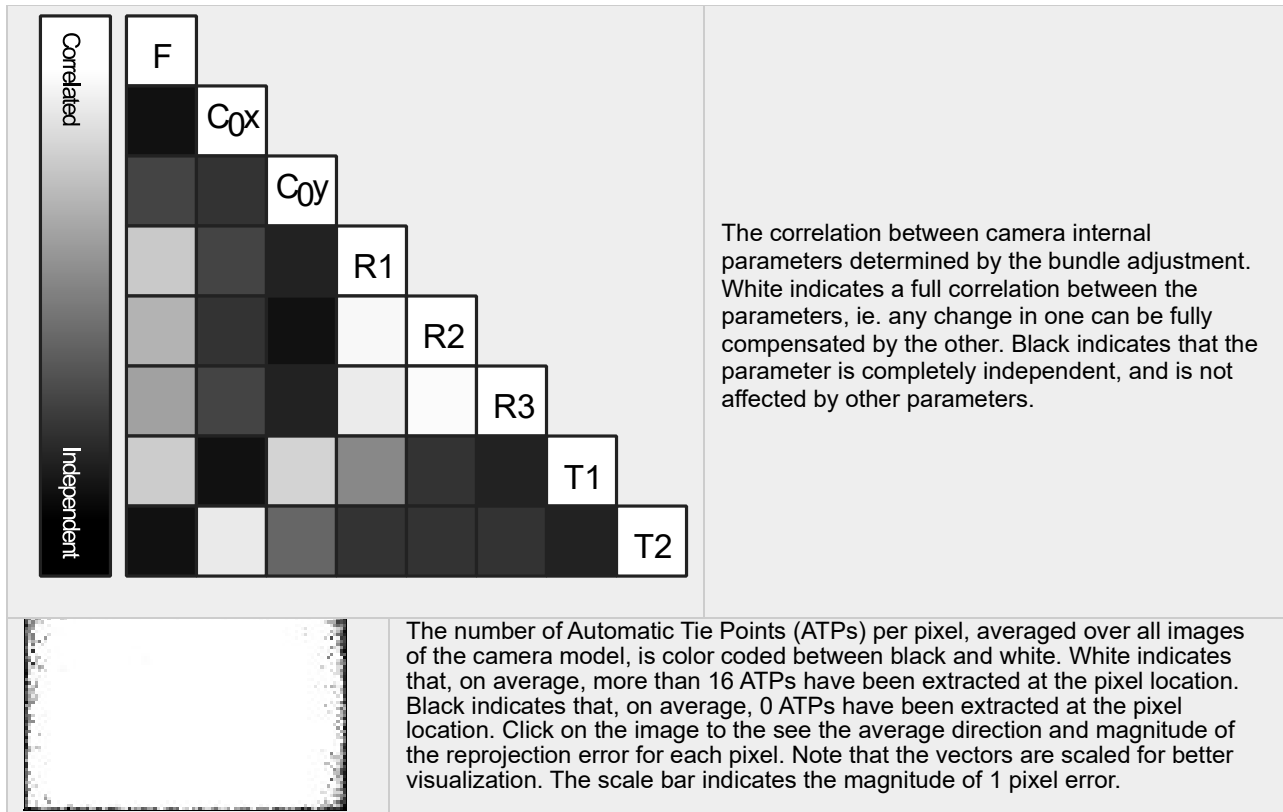


### Internal Camera Parameters

RedEdge-M\_5.5\_1280x960 (Red edge). Sensor Dimensions: 4.800 [mm] x 3.600 [mm]

EXIF ID: RedEdge-M\_5.5\_1280x960

	Focal Length	Principal Point x	Principal Point y	R1	R2	R3	T1	T2
Initial Values	1445.654 [pixel] 5.421 [mm]	637.101 [pixel] 2.389 [mm]	480.896 [pixel] 1.803 [mm]	-0.104	0.150	-0.046	0.000	-0.001
Optimized Values	1444.408 [pixel] 5.417 [mm]	638.104 [pixel] 2.393 [mm]	479.137 [pixel] 1.797 [mm]	-0.100	0.129	0.006	0.000	-0.001
Uncertainties (Sigma)	0.048 [pixel] 0.000 [mm]	0.118 [pixel] 0.000 [mm]	0.093 [pixel] 0.000 [mm]	0.001	0.005	0.011	0.000	0.000



**Camera Rig «RedEdge-M» Relatives. Images: 25825**

	Transl X [m]	Transl Y [m]	Transl Z [m]	Rot X [degree]	Rot Y [degree]	Rot Z [degree]
RedEdge-M_5.5_1280x960 (Green)	Reference Camera					
RedEdge-M_5.5_1280x960 (Blue)						
Initial Values	0.030	0.000	0.000	-0.018	0.222	0.276
Optimized values	0.030	0.000	0.000	-0.000	0.269	0.282
Uncertainties (sigma)				0.004	0.004	0.000
RedEdge-M_5.5_1280x960 (Red)						
Initial Values	0.000	0.021	0.000	0.270	-0.047	0.205
Optimized values	0.000	0.021	0.000	0.243	-0.065	0.209
Uncertainties (sigma)				0.004	0.005	0.000
RedEdge-M_5.5_1280x960 (NIR)						
Initial Values	0.030	0.021	0.000	0.123	0.077	0.250
Optimized values	0.030	0.021	0.000	0.115	0.126	0.255
Uncertainties (sigma)				0.004	0.005	0.000
RedEdge-M_5.5_1280x960 (Red edge)						

Initial Values	0.015	0.011	0.000	0.085	0.048	0.356
Optimized values	0.015	0.011	0.000	0.091	0.085	0.357
Uncertainties (sigma)				0.004	0.005	0.000

**2D Keypoints Table**



	Number of 2D Keypoints per Image	Number of Matched 2D Keypoints per Image
Median	10000	2266
Min	10000	0
Max	10000	6063
Mean	10000	2274

**2D Keypoints Table for Camera RedEdge-M\_5.5\_1280x960 (Blue)**

	Number of 2D Keypoints per Image	Number of Matched 2D Keypoints per Image
Median	10000	1440
Min	10000	0
Max	10000	5678
Mean	10000	1530

**2D Keypoints Table for Camera RedEdge-M\_5.5\_1280x960 (Green)**

	Number of 2D Keypoints per Image	Number of Matched 2D Keypoints per Image
Median	10000	2487
Min	10000	25
Max	10000	5923
Mean	10000	2520

**2D Keypoints Table for Camera RedEdge-M\_5.5\_1280x960 (Red)**

	Number of 2D Keypoints per Image	Number of Matched 2D Keypoints per Image
Median	10000	1799
Min	10000	0
Max	10000	6063
Mean	10000	1853

**2D Keypoints Table for Camera RedEdge-M\_5.5\_1280x960 (NIR)**

	Number of 2D Keypoints per Image	Number of Matched 2D Keypoints per Image
Median	10000	1507
Min	10000	0
Max	10000	5732
Mean	10000	1563

**2D Keypoints Table for Camera RedEdge-M\_5.5\_1280x960 (Red edge)**

	Number of 2D Keypoints per Image	Number of Matched 2D Keypoints per Image
Median	10000	1639
Min	10000	0
Max	10000	5680
Mean	10000	1696

### Median / 75% / Maximal Number of Matches Between Camera Models

	RedEdge-M_5.5_... (Blue)	RedEdge-M_5.5... (Green)	RedEdge-M_5.5_1... (Red)	RedEdge-M_5.5_1...(NIR)	RedEdge-M_...(Red edge)
RedEdge-M_5.5_1280x960 (Blue)	128 / 642 / 4125				
RedEdge-M_5.5_1280x960 (Green)		22 / 98 / 3598			
RedEdge-M_5.5_1280x960 (Red)			178 / 768 / 4477		
RedEdge-M_5.5_1280x960 (NIR)				128 / 618 / 4175	
RedEdge-M_5.5_1280x960 (Red edge)					149 / 674 / 4200

### 3D Points from 2D Keypoint Matches



	Number of 3D Points Observed
In 2 Images	3750253
In 3 Images	1001490
In 4 Images	435873
In 5 Images	210276
In 6 Images	119107
In 7 Images	73228
In 8 Images	48348
In 9 Images	33037
In 10 Images	23440
In 11 Images	16892
In 12 Images	12582
In 13 Images	9377
In 14 Images	7046
In 15 Images	5199
In 16 Images	3920
In 17 Images	3003
In 18 Images	2256
In 19 Images	1662
In 20 Images	1352
In 21 Images	988
In 22 Images	803
In 23 Images	669
In 24 Images	525
In 25 Images	399
In 26 Images	315

In 27 Images	258
In 28 Images	204
In 29 Images	182
In 30 Images	144
In 31 Images	96
In 32 Images	90
In 33 Images	74
In 34 Images	52
In 35 Images	44
In 36 Images	31
In 37 Images	31
In 38 Images	20
In 39 Images	19
In 40 Images	19
In 41 Images	19
In 42 Images	14
In 43 Images	6
In 44 Images	6
In 45 Images	9
In 46 Images	2
In 47 Images	4
In 48 Images	2
In 49 Images	1
In 50 Images	3
In 52 Images	2
In 53 Images	3
In 54 Images	2
In 55 Images	1
In 56 Images	1
In 58 Images	2
In 59 Images	1
In 63 Images	1
In 64 Images	1

 **2D Keypoint Matches**



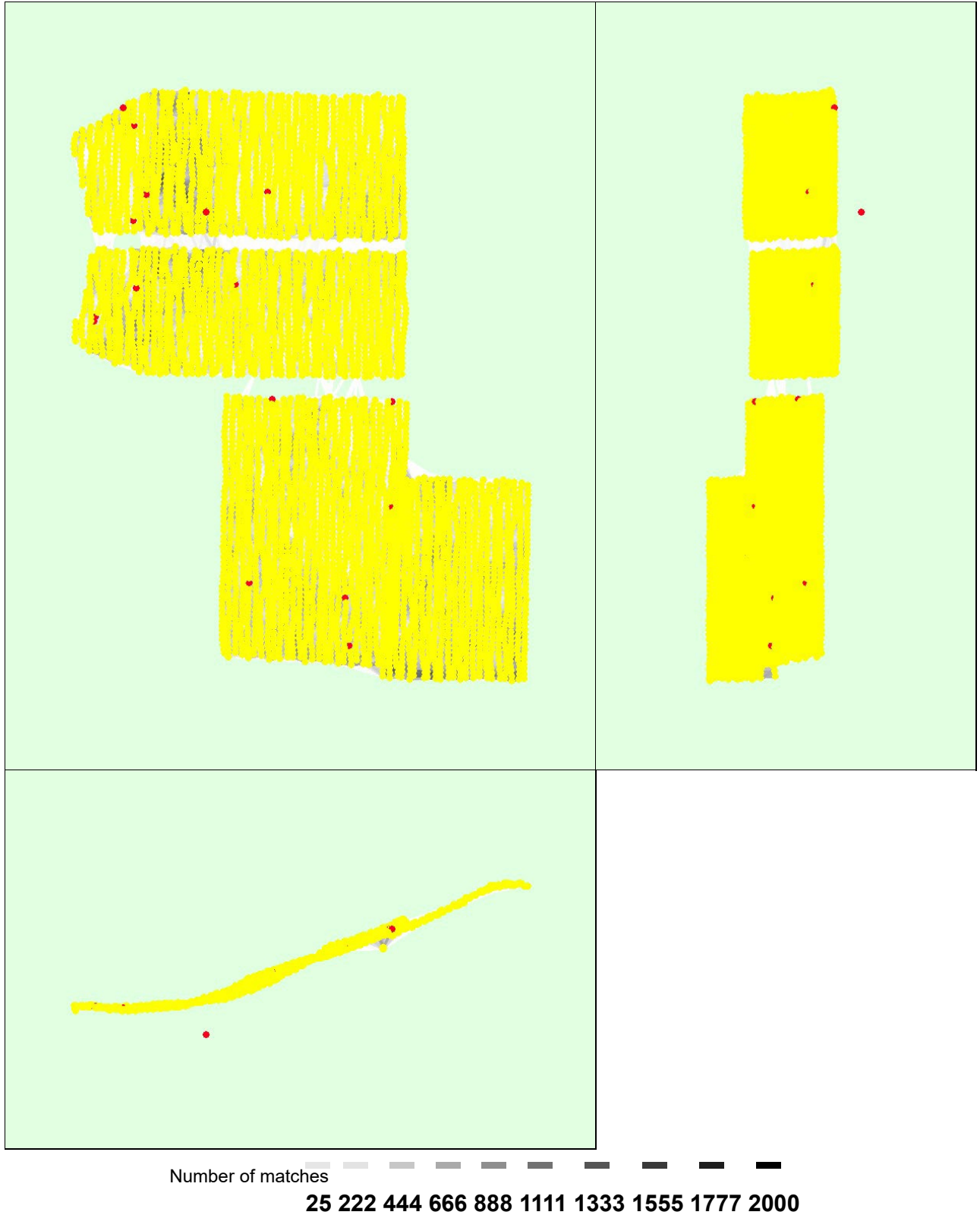


Figure 5: Computed image positions with links between matched images. The darkness of the links indicates the number of matched 2D keypoints between the images. Bright links indicate weak links and require manual tie points or more images.



# Geolocation Details



## Absolute Geolocation Variance



Min Error [m]	Max Error [m]	Geolocation Error X [%]	Geolocation Error Y [%]	Geolocation Error Z [%]
-	-1.29	0.00	0.00	0.00
-1.29	-1.03	0.00	0.00	0.00
-1.03	-0.78	0.00	0.00	0.00
-0.78	-0.52	0.00	0.00	0.00
-0.52	-0.26	0.03	0.19	0.04
-0.26	0.00	52.42	53.78	43.63
0.00	0.26	47.55	46.03	56.29
0.26	0.52	0.00	0.00	0.04
0.52	0.78	0.00	0.00	0.00
0.78	1.03	0.00	0.00	0.00
1.03	1.29	0.00	0.00	0.00
1.29	-	0.00	0.00	0.00
<b>Mean [m]</b>		-0.001034	-0.002108	0.001728
<b>Sigma [m]</b>		0.023453	0.021406	0.016366
<b>RMS Error [m]</b>		0.023476	0.021510	0.016457

Min Error and Max Error represent geolocation error intervals between -1.5 and 1.5 times the maximum accuracy of all the images. Columns X, Y, Z show the percentage of images with geolocation errors within the predefined error intervals. The geolocation error is the difference between the initial and computed image positions. Note that the image geolocation errors do not correspond to the accuracy of the observed 3D points.

## Relative Geolocation Variance



Relative Geolocation Error	Images X [%]	Images Y [%]	Images Z [%]
[-1.00, 1.00]	91.40	98.11	99.04
[-2.00, 2.00]	99.86	99.86	99.94
[-3.00, 3.00]	99.98	99.98	99.96
<b>Mean of Geolocation Accuracy [m]</b>	0.035490	0.035490	0.036850
<b>Sigma of Geolocation Accuracy [m]</b>	0.018056	0.018056	0.032345

Images X, Y, Z represent the percentage of images with a relative geolocation error in X, Y, Z.

Geolocation Orientational Variance	RMS [degree]
Omega	3.364
Phi	4.463
Kappa	5.734

Geolocation RMS error of the orientation angles given by the difference between the initial and computed image orientation angles.

# Initial Processing Details



## System Information



Hardware	CPU: AMD Ryzen Threadripper 3970X 32-Core Processor RAM: 256GB GPU: unknown graphics card (Driver: unknown)
Operating System	Windows 10 Education, 64-bit

## Coordinate Systems



Image Coordinate System	WGS 84
Output Coordinate System	WGS 84 / UTM zone 11N

## Processing Options



Detected Template	RedEdgeMX 5Band*
Keypoints Image Scale	Full, Image Scale: 2
Advanced: Matching Image Pairs	Aerial Grid or Corridor
Advanced: Matching Strategy	Use Geometrically Verified Matching: yes
Advanced: Keypoint Extraction	Targeted Number of Keypoints: Custom, Number of Keypoints: 10000
Advanced: Calibration	Calibration Method: Geolocation Based Internal Parameters Optimization: All External Parameters Optimization: All Rematch: Auto, no
Rig «RedEdge-M» processing	optimize relative rotation using a subset of secondary cameras

# Point Cloud Densification details



## Processing Options



Image Scale	multiscale, 1 (Original image size, Slow)
Point Density	Optimal
Minimum Number of Matches	3
3D Textured Mesh Generation	no
LOD	Generated: no
Advanced: Image Groups	Blue, Green, Red, NIR, Red edge
Advanced: Use Processing Area	yes
Advanced: Use Annotations	no
Time for Point Cloud Densification	54m:56s
Time for Point Cloud Classification	NA
Time for 3D Textured Mesh Generation	NA

## Results








Number of Generated Tiles	6
Number of 3D Densified Points	152826005
Average Density (per m <sup>3</sup> )	10.72

## DSM, Orthomosaic and Index Details

### Processing Options

DSM and Orthomosaic Resolution	10 [cm/pixel]
DSM Filters	Noise Filtering: no Surface Smoothing: no
Orthomosaic	Generated: yes Merge Tiles: yes GeoTIFF Without Transparency: yes Google Maps Tiles and KML: no
Raster DTM	Generated: yes Merge Tiles: yes
DTM Resolution	10 [cm/pixel]
Radiometric calibration with reflectance target	yes
Index Calculator: Reflectance Map	Generated: yes Resolution: 1 x GSD (11.2 [cm/pixel]) Merge Tiles: yes
Index Calculator: Indices	ndvi
Time for DSM Generation	00s
Time for Orthomosaic Generation	08h:08m:07s
Time for DTM Generation	00s
Time for Contour Lines Generation	00s
Time for Reflectance Map Generation	05h:45m:06s
Time for Index Map Generation	03m:49s

### Camera Radiometric Correction

Camera Name	Band	Radiometric Correction Type	Reflectance target
RedEdge-M_5.5_1280x960	Blue	Camera, Sun Irradiance and Sun Angle using DLS IMU	
RedEdge-M_5.5_1280x960	Green	Camera, Sun Irradiance and Sun Angle using DLS IMU	
RedEdge-M_5.5_1280x960	Red	Camera, Sun Irradiance and Sun Angle using DLS IMU	
RedEdge-M_5.5_1280x960	NIR	Camera, Sun Irradiance and Sun Angle using DLS IMU	
RedEdge-M_5.5_1280x960	Red edge	Camera, Sun Irradiance and Sun Angle using DLS IMU	

## **REFERENCES**

## REFERENCES

- Argamosa, R. J. L., E. C. Paringit, K. R. Quinton, F. A. M. Tandoc, R. A. G. Faelga, C. A. G. Ibañez, M. A. V. Posilero, and G. P. Zaragosa. 2016. “Fully Automated Gis-Based Individual Tree Crown Delineation Based on Curvature Values from a LiDAR Derived Canopy Height Model in a Coniferous Plantation.” *ISPRS - International Archives of the Photogrammetry Remote Sensing and Spatial Information Sciences XLI-B8* (June): 563–69.
- Avitabile, Valerio, Martin Herold, Matieu Henry, and Christiane Schmillius. 2011. “Mapping Biomass with Remote Sensing: A Comparison of Methods for the Case Study of Uganda.” *Carbon Balance and Management* 6 (October): 7.
- Cairns, Michael A., Sandra Brown, Eileen H. Helmer, and Greg A. Baumgardner. 1997. “Root Biomass Allocation in the World’s Upland Forests.” *Oecologia* 111 (1): 1–11.
- Chen, Q., and C. Qi. 2013. “- LiDAR Remote Sensing of Vegetation Biomass.” In *Remote Sensing of Natural Resources*, 424–45. CRC Press.
- Chen, Qi, Gaia Vaglio Laurin, John J. Battles, and David Saah. 2012. “Integration of Airborne Lidar and Vegetation Types Derived from Aerial Photography for Mapping Aboveground Live Biomass.” *Remote Sensing of Environment* 121 (June): 108–17.
- Di Lallo, Giulio, Philip Mundhenk, Sheila Edith Zamora López, Marco Marchetti, and Michael Köhl. 2017. “REDD+: Quick Assessment of Deforestation Risk Based on Available Data.” *Forests, Trees and Livelihoods* 8 (1): 29.
- ESRI. “Performing Supervised Object-Based Image Classification.” ESRI Academy. 2022. <https://www.esri.com/training/catalog/5c9a65e0190cf23eac628f9c/performing-supervised-objectbased-image-classification/>
- Goodbody, Tristan, R. H., C. Coops, Nicholas L. Marshall Peter, Tompalski Piotr, and Crawford Patrick. 2017. “Unmanned Aerial Systems for Precision Forest Inventory Purposes: A Review and Case Study.” *Forestry Chronicle*, March. <https://doi.org/10.5558/tfc2017-012>.
- Gurgel, Angelo. 2022. “Carbon Offsets Explained.” MIT Climate Portal. <https://climate.mit.edu/explainers/carbon-offsets>
- Houghton, R. A., Forrest Hall, and Scott J. Goetz. 2009. “Importance of Biomass in the Global Carbon Cycle.” *Journal of Geophysical Research* 114 (G2). <https://doi.org/10.1029/2009jg000935>.

- Iizuka, Kotaro, Taichiro Yonehara, Masayuki Itoh, and Yoshiko Kosugi. 2017. "Estimating Tree Height and Diameter at Breast Height (DBH) from Digital Surface Models and Orthophotos Obtained with an Unmanned Aerial System for a Japanese Cypress (*Chamaecyparis Obtusa*) Forest." *Remote Sensing* 10 (1): 13.
- Jenkins, Jennifer Caroline. 2004. *Comprehensive Database of Diameter-Based Biomass Regressions for North American Tree Species*. United States Department of Agriculture, Forest Service, Northeastern Research Station.
- Jing, Linhai, Baoxin Hu, Jili Li, and Thomas Noland. 2012. "Automated Delineation of Individual Tree Crowns from Lidar Data by Multi-Scale Analysis and Segmentation." *Photogrammetric Engineering & Remote Sensing* 78 (12): 1275–84.
- Jones, Alice R., Ramesh Raja Segaran, Kenneth D. Clarke, Michelle Waycott, William S. H. Goh, and Bronwyn M. Gillanders. 2020. "Estimating Mangrove Tree Biomass and Carbon Content: A Comparison of Forest Inventory Techniques and Drone Imagery." *Frontiers in Marine Science* 6. <https://doi.org/10.3389/fmars.2019.00784>.
- Ketterings, Quirine M., Richard Coe, Meine van Noordwijk, Yakub Ambagau', and Cheryl A. Palm. 2001. "Reducing Uncertainty in the Use of Allometric Biomass Equations for Predicting Above-Ground Tree Biomass in Mixed Secondary Forests." *Forest Ecology and Management* 146 (1): 199–209.
- Kumar, Lalit, and Onesimo Mutanga. 2017. "Remote Sensing of Above-Ground Biomass." *Remote Sensing* 9 (9): 935.
- Lefebvre, David, Adrian G. Williams, Guy J. D. Kirk, Paul, J. Burgess, Jeroen Meersmans, Miles R. Silman, Francisco Román-Dañobeytia, Jhon Farfan, and Pete Smith. 2021. "Assessing the Carbon Capture Potential of a Reforestation Project." *Scientific Reports* 11 (1): 19907.
- Lefsky, David Gwenzi Michael. n.d. "Plot-Level Aboveground Woody Biomass Modeling Using Canopy Height and Auxiliary Remote Sensing Data in a Heterogeneous Savanna." <https://doi.org/10.1117/1.JRS.10.016001>.
- Lefsky, Michael A., Warren B. Cohen, David J. Harding, Geoffrey G. Parker, Steven A. Acker, and S. Thomas Gower. 2002. "Lidar Remote Sensing of above-Ground Biomass in Three Biomes." *Global Ecology and Biogeography: A Journal of Macroecology* 11 (5): 393–99.
- Lian, Xugang, Hailang Zhang, Wu Xiao, Yunping Lei, Linlin Ge, Kai Qin, Yuanwen He, et al. 2022. "Biomass Calculations of Individual Trees Based on Unmanned Aerial Vehicle Multispectral Imagery and Laser Scanning Combined with Terrestrial Laser Scanning in Complex Stands." *Remote Sensing* 14 (19): 4715.

- Lu, Dengsheng, Qi Chen, Guangxing Wang, Lijuan Liu, Guiying Li, and Emilio Moran. 2016. “A Survey of Remote Sensing-Based Aboveground Biomass Estimation Methods in Forest Ecosystems.” *International Journal of Digital Earth* 9 (1): 63–105.
- Marino, Bruno D. V., and Nahuel Bautista. 2022. “Commercial Forest Carbon Protocol Over-Credit Bias Delimited by Zero-Threshold Carbon Accounting.” *Trees, Forests and People* 7 (March): 100171.
- Maulana, Sandhi I., Yohannes Wibisono, and Singgih Utomo. 2016. “Development Of Local Allometric Equation to Estimate Total Aboveground Biomass In Papua Tropical Forest.” *Indonesian Journal of Forestry Research* 3 (2): 107–18.
- Mlambo, Reason, Iain H. Woodhouse, France Gerard, and Karen Anderson. 2017. “Structure from Motion (SfM) Photogrammetry with Drone Data: A Low Cost Method for Monitoring Greenhouse Gas Emissions from Forests in Developing Countries.” *Forests, Trees and Livelihoods* 8 (3): 68.
- Ngomanda, Alfred, Nestor Laurier Engone Obiang, Judicaël Lebamba, Quentin Moundounga Mavouroulou, Hugues Gomat, Géraud Sidoine Mankou, Joël Loumeto, et al. 2014. “Site-Specific versus Pantropical Allometric Equations: Which Option to Estimate the Biomass of a Moist Central African Forest?” *Forest Ecology and Management* 312 (January): 1–9.
- OpenAI. 2024. “Explanation of Texture in Remote Sensing.” GPT (Generative Pre-trained Transformer) - ChatGPT.
- OpenAI. 2024. “Forests versus Woodlands.” GPT (Generative Pre-trained Transformer) – ChatGPT.
- Pillsbury, Norman H., and Michael L. Kirkley. 1984. “Equations for Total, Wood, and Saw-Log Volume for Thirteen California Hardwoods.” Vol. 414. Portland, OR: U.S. Department of Agriculture, Forest Service, Pacific Northwest Forest and Range Experiment Station. <https://doi.org/10.2737/pnw-rn-414>.
- Wallace, Luke, Arko Lucieer, Zbyněk Malenovský, Darren Turner, and Petr Vopěnka. 2016. “Assessment of Forest Structure Using Two UAV Techniques: A Comparison of Airborne Laser Scanning and Structure from Motion (SfM) Point Clouds.” *Forests, Trees and Livelihoods* 7 (3): 62.
- Weiskittel, Aaron R., David W. MacFarlane, Philip J. Radtke, David L. R. Affleck, Hailemariam Temesgen, Christopher W. Woodall, James A. Westfall, and John W. Coulston. 2015. “A Call to Improve Methods for Estimating Tree Biomass for Regional and National Assessments.” *Journal of Forestry* 113 (4): 414–24.

Xu, Zhong, Xin Shen, Lin Cao, Nicholas C. Coops, Tristan R. H. Goodbody, Tai Zhong, Weidong Zhao, et al. 2020. "Tree Species Classification Using UAS-Based Digital Aerial Photogrammetry Point Clouds and Multispectral Imageries in Subtropical Natural Forests." *International Journal of Applied Earth Observation and Geoinformation* 92 (October): 102173.

Zhao, Houben, Zhaojia Li, Guangyi Zhou, Zhijun Qiu, and Zhongmin Wu. 2019. "Site-Specific Allometric Models for Prediction of Above-and Belowground Biomass of Subtropical Forests in Guangzhou, Southern China." *Forests, Trees and Livelihoods* 10 (10): 862.